DESIGN AND TESTING OF AN ORTHOGONAL LCP INTERCONNECT FOR RF APPLICATIONS IN HIGH VIBRATION ENVIRONMENTS

A Thesis
Presented to
The Academic Faculty

by

Luca Guidoni

In Partial Fulfillment
of the Requirements for the Degree
Master's of Science in the
School of Aerospace Engineering

Georgia Institute of Technology
May 2016

Copyright © Luca Guidoni 2016

DESIGN AND TESTING OF AN ORTHOGONAL LCP INTERCONNECT FOR RF APPLICATIONS IN HIGH VIBRATION ENVIRONMENTS

Approved by:

Dr. Massimo Ruzzene, Advisor
School of Aerospace Engineering
Georgia Institute of Technology

Dr. Minfeng Yu
School of Aerospace Engineering
Georgia Institute of Technology

Dr. Julian J. Rimoli
School of Aerospace Engineering
Georgia Institute of Technology

Dr. Graeme Kennedy
School of Aerospace Engineering
Georgia Institute of Technology

Date Approved: 1/29/2016

ACKNOWLEDGEMENTS

I wish to thank the team at Harris Corporation, particularly: Brinnan Riley, Bill Clark, Tom Wells and Dr. Louis Rendek for the incredible support through this investigation, and for granting me an invaluable learning experience through my Harris internship. I would also like to extend a thank you to my advisor Dr. Massimo Ruzzene for allowing me to be a member of his team since my undergraduate years, and for advising me throughout my graduate studies.

TABLE OF CONTENTS

	Page
ACKNOWLEDGEMENTS	iii
LIST OF TABLES	vi
LIST OF FIGURES	vii
LIST OF SYMBOLS AND ABBREVIATIONS	x
SUMMARY	xi
CHAPTER	
1 INTRODUCTION AND MOTIVATION	1
1.1 The Problem of Orthogonal Interconnection	1
1.2 Available Solutions and Literature Review	3
1.3 The Advantages of LCP	5
1.4 Motivation and Objectives	7
1.5 Organization of Thesis	9
2 INTERCONNECT SPRING DESIGN	10
2.1 Early Studies and Concepts	10
2.2 Clamped-Free Arc Spring Design	11
2.2.1 Analytical Estimation of Stress Distribution	11
2.2.2 Numerical Estimation of Stress Distribution	14
2.3 Semicircular Spring Design	17
2.3.1 Analytical Estimation of Stress Distribution	17
2.3.2 Numerical Estimation of Stress Distribution	21
2.4 Trade Study: Elliptical Spring with Varying Aspect Ratio	24
2.5 Optimization Studies in Confirmation of Analytical Results	28

2.6 Design Towards Fabrication: Effect of Plating on Stress Distribution 29
2.7 Design Refinement for Side Mounting to the Post 32
2.8 Conclusions 35
3 INTERCONNECT PROTOTYPE MANUFACTURING 37
3.1 Manufacturing Technique: Introduction to Thermoforming 37
3.2 Breadboard Tests and Initial Trials 38
3.3 Tooling Design and Fabrication 42
3.4 Spring Thermoforming Results 46
3.5 Interconnect Final Assembly 49
3.6 Conclusions 52
4 EXPERIMENTAL PERFORMANCE VALIDATION 53
4.1 Setup Requirements, Component Selection, and Fabrication 53
4.2 Digital Acquisition Logic 59
4.3 Excitation Setup and Monitoring 61
4.4 Results: Performance Under Axial Cyclic Loading 62
4.5 Results: Performance Under Horizontal Cyclic Loading 68
4.6 Conclusions 69
5 CONCLUSIONS AND FUTURE WORK 71
5.1 Summary 71
5.2 Contributions 73
5.3 Future Work 74
REFERENCES 76

LIST OF TABLES

	Page
Table 1: Design Requirements for the Experimental Setup	53
Table 2: Summary of the Excitation Setup for Axial Loading	62
Table 3: Summary of the Excitation Setup for Horizontal Loading	62
Table 4: Summary of Axial Testing Results	66
Table 5: Summary of Horizontal Testing Results	69

LIST OF FIGURES

Page

Figure 1: Prototype LCP microstrip-to-microstrip transition in (a) Planar configuration (b) Orthogonal configuration 6

Figure 2: Design Problem Statement Showing Perpendicular Boards That Must Be Joined with Interconnect Springs. Vertical Origin Line Shown as Dashed. 10

Figure 3: 90° Circle Arc Interconnect Design Rendering 12

Figure 4: Proposed Geometry (Left) and Simplified Model (Right) For a 90° Circular Arc Interconnect 12

Figure 5: 2D Von Mises Stress Distribution in 90° Arc Connector Cross Section due to 8 mil Total Applied Displacement 15

Figure 6: 3D Von Mises Stress Distribution in 90° Arc Connector Copper layer (Right) and Side View Zoom (Right) due to 8 mil Total Applied Displacement 16

Figure 7: Simply Supported Curved Beam Model with Applied Axial End Load 18

Figure 8: Infinitesimal Curved Beam Section with Geometry and Applied Moments Labeled 19

Figure 9: Analytical Peak Stress Location of Proposed Semicircular Spring Design 20

Figure 10: Cross Section Composition for Copper-Clad LCP 20

Figure 11: Von Mises Stress Distribution vs. Curvilinear Co-Ordinate in the Copper Layer for 2D Plane Stress Semicircular Interconnect Model due to 8 mil Total Applied Displacement 22

Figure 12: Deformed Shape (shaded) Superimposed on Undeformed Shape (outline) of Semicircular Interconnect Under 8 mil Total Applied Displacement 23

Figure 13: 3D Von Mises Stress Distribution in Semicircular Connector Under 8 mil Total Applied Displacement 23

Figure 14: Von Mises Stress Distribution vs. Curvilinear Co-Ordinate in the Copper Layer for 2D Plane Stress Interconnect with Aspect Ratio of 2 due to 8 mil Total Applied Displacement 25

Figure 15: Von Mises Stress Distribution vs. Curvilinear Co-Ordinate in the Copper Layer for 2D Plane Stress Interconnect with Aspect Ratio of 2 due to 8 mil Total Applied Displacement 26

Figure 16: Variation of Peak Von Mises Stresses in Copper Layer with Ellipse Aspect Ratio with Quadratic Interpolation 27

Figure 17: 3D Von Mises Stress Distribution in Interconnect with Aspect Ratio of 2 Under 8 mil Total Applied Displacement 27

Figure 18: 3D Von Mises Stress Distribution in Interconnect with Aspect Ratio of 0.5 Under 8 mil Total Applied Displacement 28

Figure 19: Stackup of Layers Composing the LCP Interconnect Cross-Section 30

Figure 20: Von Mises Stress Distribution vs Curvilinear Co-Ordinate from 2D FEA Simulation for 50 µIn Au (Left) and 100 µIn Au (Right) over 250 µIn Ni 30

Figure 21: Rendering of the Modified Spring Design for Side Mounting 32

Figure 22: Von Mises Stress Distribution vs. Curvilinear Co-Ordinate for 2D Plane Stress Revised Interconnect Model due to 8 mil Total Applied Displacement 33

Figure 23: Schematic of Dielectric Hard Stop Incorporation on the Tip of the Post 35

Figure 24: Layout and Groove Diameters of Thermoforming Breadboard 38

Figure 25: Thermoforming Breadboard and Corresponding Gauge Pins with the Bottom Two LCP Strips Mounted and the Top Two Unmounted After Forming 39

Figure 26: Microsections and Measured Internal Radius (mils) at 50x Magnification for (A) 63 mil diameter (B) 46 mil diameter (C) 24 mil diameter 40

Figure 27: Microsections and Measured Copper Thickness (µm) at 500x Magnification for 41

Figure 28: Rendering and Schematic of the Negative LCP Forming Mold 42

Figure 29: Rendering and Schematic of the Positive LCP Forming Mold 43

Figure 30: Printed Wiring Board (PWB) Layout for 8 Sets of LCP Springs 44

Figure 31: Cutting Diagram for Laser Singulation of Spring PWB 45

Figure 32: Fabricated PWB for 8 Sets of LCP Springs Before Singulation and Forming 46

Figure 33: Resulting Formed Shape After First Trial of Spring Forming with Two Part Mold 46

Figure 34: Rendering of the Hybrid Negative Mold with Gauge Pin 48

Figure 35: LCP Spring Formed With Hybrid Mold Using a 0.028” Gauge Pin 48

Figure 36: LCP Spring Formed With Hybrid Mold Using a 0.030” Gauge Pin 48

Figure 37: Rendering of a Single PWB for Mounting of LCP Springs on the Test Fixture 50

Figure 38: (A) Rendering of the Wraparound Assembly Technique (B) Installed Springs Using Wraparound Technique 51

Figure 39: Interconnect Prototype with Individually Installed Springs 51

Figure 40: Machined Two-Part Shaker Adapter (right) and Rendered Interconnect Assembly on the Adapter (left) 54

Figure 41: Rendering of the Secondary Adapter Plate for Horizontal Fatigue Testing 54

Figure 42: First Mode of the Horizontal Test Fixture at 1.2 kHz from COMSOL Simulation 55

Figure 43: Mating Side Printed Circuit Board for Axial Testing 56

Figure 44: Mating Side Printed Circuit Board for Horizontal Testing 57

Figure 45: Side View Rendering of Assembled Unmated Experimental Setup 58

Figure 46: Experimental Setup, Mated with All Components in Operation 58

Figure 47: Digital Acquisition Logic Diagram for Experimental Setup 59

Figure 48: Breadboard Schematic of Acquisition Logic Circuit and Monitoring Sensors 60

Figure 49: Condition of a Single Copper Spring After 15 Million Cycles of Axial Loading at 4x Magnification. (a) Side View Showing No Damage to Metallic Layer, (b) Top-Down View Showing Wear 63

Figure 50: Side View of Failed Plated Spring after 18 Million Cycles at 4x Magnification 65

Figure 51: Back View of Crack (Circled) Initiating in the Gold Layer of a Spring after 18 Million Cycles at 4x Magnification 65

Figure 52: Condition of the Mating Board After a Combined 25 Million Cycles at 4x Magnification. 67

Figure 53: Condition of the Revised Electroplated Mating Board after 80 Million Cycles in Transverse Excitation at 4x Magnification 68

Figure 54: Top-Down View at 4x Magnification of a Single Spring Showing Gold Wear after 80 Million Cycles in Transverse Excitation 69

LIST OF SYMBOLS AND ABBREVIATIONS

σ	Normal Stress
ε	Normal Strain
δ	Applied Displacement
E	Young's Modulus of Elasticity
H_{33}	Cross-Sectional Bending Stiffness
X_{2c}	x-Coordinate of the Modulus Weighted Cross-Sectional Centroid
t	Thickness
S	Axial Stiffness
R	Outer Radius
r	Inner Radius
θ	Angle of Circle Arc Swept
y	Distance from Neutral Axis
F	Frequency
D	Peak-To-Peak Displacement
A	Acceleration Amplitude
DoF	Degrees of Freedom
LCP	Liquid Crystal Polymer
1 mil	0.001 in
1 µin	$1x10^{-6}$ in
DAQ	Data Acquisition System
DC	Direct Current
ENIG	Electroless Immersion Nickel-Gold
FEA	Finite Element Analysis

SUMMARY

A new design is presented for a wideband orthogonal interconnect between two perpendicular printed wiring boards, employing novel geometries and materials to minimize stress under cyclic loading. This will ensure fatigue survivability in high vibration environments, opening the door to vertical interconnection in RF circuit design. This is, to the best of knowledge, the first complete design and prototype for an orthogonal interconnect at the board level for broadband RF circuits. An analytical approach is used to define the driving parameters in the stress distribution within a smooth curve joining two perpendicular surfaces using analytical geometries, and Finite Element Analysis is used to finalize the design and ensure all constituent materials in the interconnect are subjected to stresses below their fatigue strength at 10 million cycles at full deflection. A manufacturing process is then proposed using thermoforming to shape the Liquid Crystal Polymer base material into the desired geometry, as well as an assembly solution to mount the interconnect to an RF signal feed card. Finally, a test setup is designed allowing for high cycle fatigue testing within the order of hours, including the capability to monitor performance of the interconnect by tracking DC continuity through a simulated application using a single post design. The prototype interconnect is tested to failure and is shown to survive 18 million cycles of a typical loading application before failure of the LCP springs occurs in the mode predicted by the initial FEA model.

CHAPTER 1

INTRODUCTION AND MOTIVATION

1.1 The Problem of Orthogonal Interconnection

Interconnect technology between circuits and various components is essential in RF front end applications, specifically in regards to connecting a signal feed card to a radiating aperture. Current research and development of RF interconnects is heavily focused on planar or semi-planar transitions, which limits the number of packaging configurations available to circuit designers. For antenna design, vertical assembly allows for a significant reduction in the device's cross-sectional footprint, and would provide a cleaner installation solution with a reduced number of transitions and easier access to the individual components. The availability of a reliable orthogonal interconnect can open the door to many innovative packaging solutions, removing design restrictions and allowing an increase in performance and compactness of the final appliance, as well as facilitating assembly and maintainability. Vertical interconnection presents many challenges from the structural point of view, primarily with regards to load bearing capabilities of the connector, which now becomes an integral part of the overall structure, and susceptibility to vibrations. A uniform preload must be insured on all components of the interconnect during installation, which might include blind mating between the feed card and the aperture board. Locating the two boards in the correct alignment is crucial to ensure a solid and resilient connection: the load bearing nature of the interconnect means that a non-uniform load distribution throughout the individual interconnect or the various interconnects along the entire card will result in premature failure of the components, especially if subject to cyclic vibration loads. Such an appliance would also need to

survive several mating and de-mating procedures for maintenance purposes, which impose further loads throughout the product lifecycle.

Current state of the art in orthogonal interconnect technology is limited, and has always proposed a trade-off between RF performance and mechanical resilience, as very few of the applications using this type of interconnection see operations in high vibration environments. Often a design with excellent RF performance has poor mechanical properties as the driving geometric parameters for the two goals do not necessarily align. This study aims to design and validate an orthogonal interconnect for use in high-vibration environments, and will therefore present a design which eliminates this tradeoff providing a good compromise between RF and fatigue performance. Focus will be on the mechanical performance of the interconnect appliance under high cycle fatigue due to cyclical loading. To achieve this goal, a geometry was developed in collaboration with RF engineers at Harris Corporation and the Microwave Circuit Technology Group at Georgia Tech, led by Dr. John Papapolymerou, to satisfy the performance requirements in both fields, and novel materials were implemented, particularly the use of metalized Liquid Crystal Polymer (LCP) which sees its first use in this application.

A further difficulty in designing a reliable, high performing orthogonal interconnect is a stringent manufacturing requirement on the feed card. The feed card in a typical application is designed to have several posts that extend towards the radiating aperture onto which the interconnect is mounted. These posts have a very tight manufacturing tolerances to ensure spacing between the two cards is constant. After the feed card geometry is cut out of the dielectric material, the length of the posts is adjusted by passing the entire card with the post side down over a routing bit, which grinds off the tips of the posts to achieve a uniform length, within 0.001” tolerance. This manufacturing process is the only one that allows machining of the cards within the desired tolerance, but introduces the requirement that the RF signal must enter the interconnect through the sides of the posts, as a bottom connection point is not possible due to the routing step.

Such a mounting requirement introduces yet more complexity in the design, but must be satisfied by the final appliance.

1.2 Available Solutions and Literature Review

Orthogonal interconnection of circuit boards has been used in circuit design since the early adoption of transistor based circuits and really began manifesting its advantages in electronics packaging with the miniaturization race sparked by the adoption of microprocessors. Notable examples include the interconnection between mother and daughter boards using pin type connections, either directly as a feature on the circuit board itself or through a flexible ribbon-type interconnect. Specific examples of these interconnect technologies have been patented since the 1980s, such as the orthogonal interconnects proposed by Andre Petit, Etienne Penicaud, et. al [1] in 1986, or an elastomeric mother-daughter board interconnect proposed also in 1986 by Donald G. Stillie [2]. Design refinements of these interconnect designs have been made through the years to warrant better performance, such as the design patented by Herman Kwong et. al in 2000 [3], but all substantially use the same pin architecture to interconnect the two boards, due to it being a reliable and proven solution. All orthogonal interconnect applications have been limited to ohmic type connections for digital circuits, such as those used in most consumer electronics, and have yet to see an expansion to analog and RF circuits, due to the completely different parameters to characterize the electrical performance of the interconnect.

In the realm of RF circuit design, interconnects have been limited in the past to planar or semi-planar transitions, with some interest in the past 15 years being devoted to the development of vertical interconnects, due to the space saving advantages from the packaging point of view that can promote miniaturization of devices. These interconnection techniques were demonstrated between integrated RF circuits by Goverdhanam, Simons, and Katehi [4], and characterized for individual dies and wafers

by Newman et. al [5] with regards to their electrical performance. A general overview of vertical interconnection technology was given in 2005 by Davis et. al. [6] from the design point of view, presenting the pros and cons of the mainstream vertical interconnection techniques which included: wire bonding, microbumps, through vias, and contactless or AC coupled interconnection. All of the vertical interconnection methods mentioned for RF circuits have one feature in common: they are all methods for 3D interconnection of parallel boards, and do not allow for interconnection between orthogonal boards. To further increase packaging possibilities, it is therefore desirable to incorporate orthogonal interconnection methods, as has been done for many years in the digital circuit realm, to RF circuit design.

While academic literature in this regard is lacking, designs have been attempted in industry research and development which have yet to be published. Although specific details cannot be provided due to proprietary restrictions, and knowledge of what is being investigated within other companies is restricted, Harris Corporation has explored some initial concepts that lead to the request for this investigation. The concept involves a horizontal card with contact pads and a perpendicular card with protruding posts in a regular pattern. An RF signal is routed from the card down through the posts. The posts will be interconnected to their corresponding contact pad on the horizontal card. A more detailed explanation of the card geometries will be given in Chapter 2 of this thesis. An initial prototype was developed at Harris with a Beryllium-Copper spring-type interconnect feature fixed to the horizontal card onto which the posts on the vertical card would mate, and while the concept exhibited good RF performance, it failed prematurely under fatigue and is therefore not acceptable in a high vibration environment. This investigation maintains the post architecture on the perpendicular card, but plans to incorporate the interconnect features to the posts themselves, which will then mate to the horizontal board providing better mechanical performance and easier control of the loads imparted on the interconnect itself. This thesis also focuses on using metalized Liquid

Crystal Polymer (LCP) as the constituent material for the interconnect. In a parallel internal investigation within Harris, a new interconnect is being designed maintaining Beryllium-Copper as the constituent material but changing the interconnect fixture point to the post as well.

1.3 The Advantages of LCP

It is desirable to utilize a flexible base material that will offer improved compliance under load, and design a configuration which minimizes stresses within the connector to maintain levels below the fatigue strength of the individual component materials. Liquid Crystal Polymer (LCP) is a thin and flexible material which can be metal plated, and exhibits low dielectric losses at high frequencies, providing excellent RF performance for wideband applications. Qiu et. al. [7] and Sloan et. al. [8] demonstrated excellent fatigue behavior of LCP under cyclic loading, by showing how adding a percentage of LCP fibers to flexible polymer blends increase the fatigue performance of the overall polymer. This result shows that it a suitable candidate for the proposed application in high vibration environments. Furthermore, the resilient behavior of LCP is further confirmed by Voss and Freidrich [9], who experimentally verified that additional short fiber reinforcement actually decreases the performance of LCP under fatigue, due to poor matrix-fiber bond strength. Liquid Crystal Polymer therefore possesses very desirable standalone mechanical and electrical properties.

From the RF point of view, the great RF performance at microwave frequencies was experimentally demonstrated by Thompson et. al. [10] in a test that returned very low insertion and return losses in the microwave band. Due to the promising electromechanical properties of this material, as well as it being biocompatible, LCP is currently being pursued in many biomedical RF applications and is seeing increased use in biomedical interconnect designs, such as the implant interconnect proposed by Dean

et. al [11]. It has also been used successfully in a vertical interconnect application for a wireless sensor, also in the biomedical world, by Ha, Kim, et. al [12].

In seeking better characterization of LCP dielectric properties to gauge applicability for an orthogonal RF interconnect, McQuaide et. al. [13] experimentally measured dielectric losses in an orthogonal transition in 2014, with the production of an orthogonal microstrip-to-microstrip transition using a small strip of Rogers 3001 LCP with ½ oz. copper cladding, as shown in Figure 1.

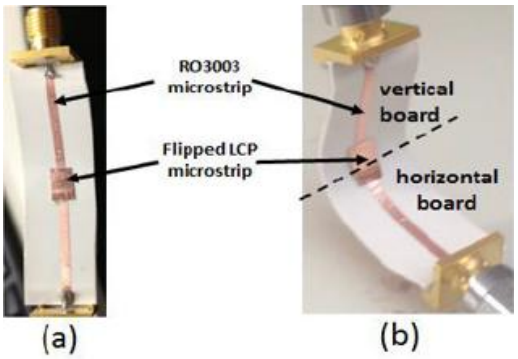

Figure 1: Prototype LCP microstrip-to-microstrip transition in (a) Planar configuration (b) Orthogonal configuration

This study, carried out in Dr. Papapolymerou's group as part of this joint investigation into orthogonal interconnects but focusing on the RF side, was vital in the continuation of the LCP interconnect design as it proved that RF performance goals could be met by such an appliance, allowing the continuation of investigation on the driving parameters to minimize peak stresses and ensure appropriate mechanical performance for fatigue survival. It was also the first time a wideband orthogonal interconnect at the board level had been demonstrated. The prototype was tested for performance in transmitting an RF signal from DC to 12 GHz, and showed low insertion and return losses throughout the entire band. Specifically, insertion loss remained below 0.5 dB/cm up to 10 GHz, demonstrating excellent performance in the desired application.

Furthermore, the most advantageous property of LCP for the purpose of this investigation is its thermoplastic properties. Due to its nature as a composite with liquid crystal fibers in a polymer matrix, the base material is sensitive to heat, and can therefore be molded using a thermoforming process, in which heat and pressure are applied to soften the material and form it into the desired shape using a mold. The LCP will retain its formed shape when returned to ambient condition, as the process does not alter fiber orientation and the fiber-matrix interface. Thermoforming of LCP with metallic cladding into complex features has been demonstrated without damage to the metal layer, and the process will be discussed in more detail in the manufacturing chapter. This property of LCP allows to manufacture interconnects with complex geometries, with very few restrictions on feature size and shape, as long as a mold can be manufactured. Compared to traditional metal shaping techniques that would have to be used for a purely metallic interconnect, such as the original Beryllium-Copper prototypes, thermoforming allows for greater flexibility in the design phase, placing fewer restrictions on the geometry due to manufacturing process. The driving factors in the stress distribution within an interconnect subject to cyclic axial and transverse loading can be analyzed and geometry can be optimized accordingly, achieving significant freedom in the design phase. Residual stresses due to manufacturing are also expected to be lower from a thermoforming process, increasing longevity of the formed part.

1.4 Motivation and Objectives

The purpose of this thesis is to propose a design for an orthogonal interconnect at the board level for RF circuits to be mounted on the posts of the vertical card and allowing connection to the horizontal card. Specific attention will be paid to mechanical performance under cyclic loading, allowing for applications in high vibration environments. Using the research carried out on the mechanical and dielectric properties of Liquid Crystal Polymer, it has been decided that it will be the constituting material for

the interconnect device. A typical application that would require such an interconnect device would operate in an environment with the following mechanical loads and requirements:

- Preload deflection of 0.004”
- Cyclic deflection of $\pm$ 0.004” amplitude
- Interconnect must allow for blind mating and demating of the two boards
- Typical misalignment between the two boards of 0.01-0.015”.
- Approximately 35 million cyclic deflection cycles throughout appliance lifetime
- Interconnect must not degrade due to motion induced wear
- Operation must be ensured in high humidity and corrosive environments

Based on these requirements, the following four baseline objectives have been identified which ensure performance of the interconnect is within the order of magnitude of desired performance. Achievement of these four goals is deemed sufficient to claim the investigation as successful, and they are the following:

1. An interconnect geometry will be designed, meeting all dimensional requirements of a typical application, such that the peak stresses in each layer due to combined static and dynamic loading will be below the materials’ respective fatigue strength at 10^7 cycles.
2. The interconnect shall be producible using current state of the art manufacturing techniques and processes.
3. The prototype interconnect shall survive a minimum of 10 million cycles under vibration testing in both axial and transverse direction.
4. A test setup will be created that successfully monitors interconnect performance and accurately identifies the moment of failure

As the project is industry sponsored, it is desired that the outcome of the investigation lead to findings that can be utilized in a future production item. Therefore, the following

3 secondary goals have also been identified which would be desirable from the industry point of view and not just as a concept demonstrator:

1. The interconnect design shall be fit for mass production
2. The prototype interconnect shall survive more than 35 million cycles under vibration testing in both axial and transverse direction.
3. The interconnect shall have RF performance greater than or equal to current state of the art planar and vertical interconnect designs

1.5 Organization of Thesis

Chapter 1 is an introduction where the details of the problem are presented, as well as a brief overview of current interconnect technology in digital and RF applications. A basic introduction to the mechanical and dielectric features of LCP is also presented, motivating the choice of this material as a constituent for the interconnect appliance. Finally, the motivation and objectives of the thesis are presented.

Chapter 2 covers the design of an orthogonal interconnect appliance, beginning with the Harris initial concept, proceeding to an initial clamped-free arc design and then to a final semicircular design based on the limitations of the clamped-free solution. Analytical and Numerical solutions are presented for the stress distribution in each configuration, and a final design refinement is made to meet manufacturing requirements.

Chapter 3 details the thermoforming technique used to manufacture an initial prototype, with details provided on how the process was specifically tailored for the application and how tooling was designed. A description of the final process and prototype assembly are given.

Chapter 4 covers testing of the prototype to experimentally validate its performance. The setup is explained in detail as well as fabrication of all components and results are presented for both axial and horizontal deflection cases.

CHAPTER 2

INTERCONNECT SPRING DESIGN

2.1 Early Studies and Concepts

Trade studies performed at Harris Corporation regarding the RF performance of orthogonal interconnect architectures showed that a spring finger type connection provided the lowest insertion and return losses between the post and the radiating surface. Contrarily to simple Ohmic connections, a vertical pin or spring type interconnection, while being mechanically very resilient, creates very high losses and is not suitable for RF use. They would also require mounting to pads on the tip of the post which is not possible given the manufacturing constraints outlined in the introduction. A general rule of thumb can be defined by stating that the conducting surfaces in the interconnect should not be in direct line of sight of each other, as that amplifies losses. Therefore, to achieve a spring finger design with acceptable RF performance, a single line must be drawn between the two perpendicular surfaces that crosses the vertical origin line as few times as possible, ideally never. The problem statement can be seen in Figure 2, with the yellow areas representing the contact pads that must be joined by the interconnect. Specific dimension will be omitted in this discussion as they are Harris proprietary.

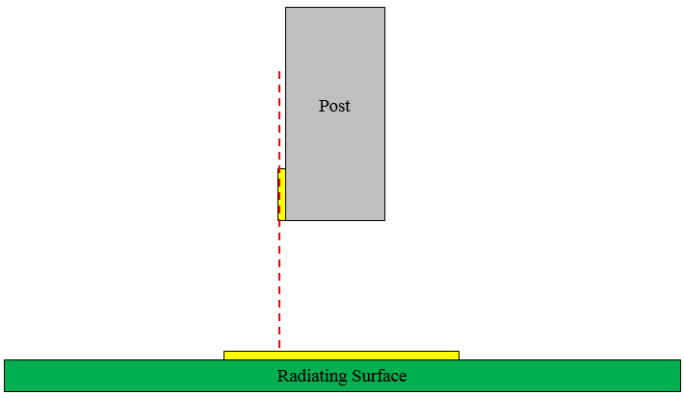

Figure 2: Design Problem Statement Showing Perpendicular Boards That Must Be Joined with Interconnect Springs. Vertical Origin Line Shown as Dashed.

Post-failure analysis of early Beryllium-Copper spring finger designs that incorporated this RF design philosophy, but were fixed to the horizontal radiating surface instead of the vertical post, showed crack initiation and subsequent failure in areas of sharp geometric discontinuity, where the spring was bent to create a sharp corner with very small radius. Furthermore, location of the interconnect spring onto the aperture side made for difficult mating of the vertical board, resulting in uneven preload on the spring fingers. While the stress discontinuity due to sharp geometry changes are a contributing factor to failure, another contributing factor is the possibility that one spring endured significantly more preload than the others, motivating the decision to locate the interconnect springs in the new design on the post itself. In order to provide adequate mechanical performance as well as RF performance, the above design must be achieved with a smooth curve, with as few bends as possible while still allowing side mounting to the post. One of the main reasons to investigate the use of LCP is that the thermoplastic properties of the constituting polymer allows for thermoforming into complex geometries, reducing manufacturing restrictions on the design. All following designs are based on a 4 mil thick LCP with ½ oz. rolled Copper cladding. Manufacturing process development and tooling design will be discussed in the next chapter addressing the finalized design.

2.2 Clamped-Free Arc Spring Design

2.2.1 Analytical Estimation of Stress Distribution

An initial proposition involved a 90 degree circle arc that would mount to the side of the post via a straight section of the same dimensions as the post's solder pads and allow perpendicular connection to the radiating surface. A rendering of this spring design is shown in Figure 3, without the post present but showing the radiating surface contact.

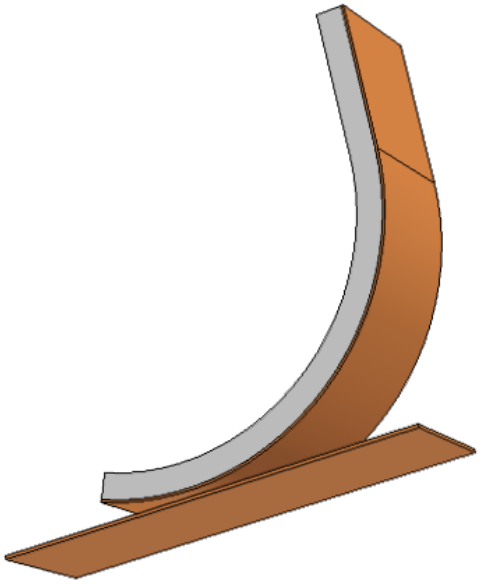

Figure 3: 90° Circle Arc Interconnect Design Rendering

Such a geometry can be approximated as a right angle bracket for the purposes of analytically defining its behavior under compressive loading and the resulting stress distribution, as shown in Figure 4.

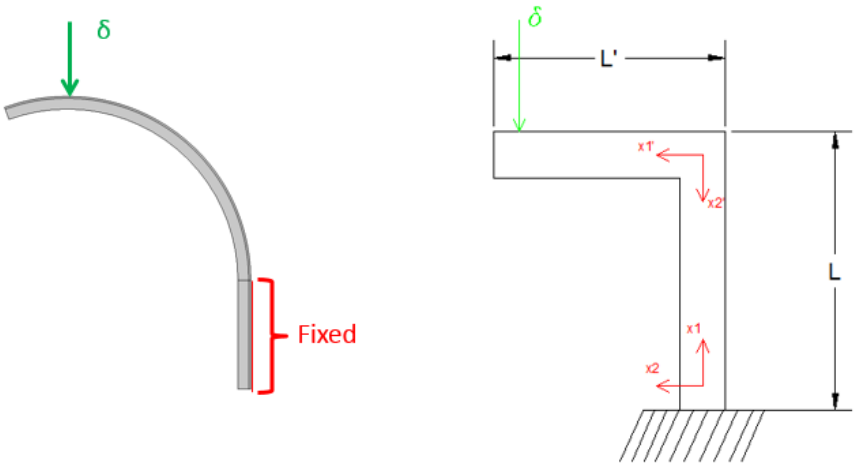

Figure 4: Proposed Geometry (Left) and Simplified Model (Right) For a 90° Circular Arc Interconnect

The bracket representation was solved analytically by applying a displacement δ at the tip and solving for the peak stresses in each constitutive layer of the cross-section. Pure bending was assumed, yielding an expression for the peak stress due to bending in each layer of the connector's cross-section. For each case, the peak normal stresses occur at the root, where the bracket is fixed, and can be found as follows:

$$\sigma_{max}{}^{cu} = \frac{12E_{cu}\delta}{L'^2}\left[\frac{H_{33}}{L'S} + (t_{cu} + x_{2c})(\frac{1}{2} + \frac{x_{2c}}{L'})\right]$$
$$\sigma_{max}{}^{lcp} = \frac{12E_{lcp}\delta}{L'^2}\left[\frac{H_{33}}{L'S} + (x_{2c} - t_{lcp})(\frac{1}{2} + \frac{x_{2c}}{L'})\right] \quad (1)$$

In Equation 1 above, E represents the Young's Modulus of the subscripted layer, H_{33} is the bending stiffness of the cross section, X_{2c} is the x-coordinate of the modulus weighted cross-sectional centroid, t represents the thickness of the subscripted layer, S is the axial stiffness and L and L' are as marked in Figure 4. Explicit derivations for the quoted quantities is given below in equation set 2:

$$S = E_{lcp}t_{lcp} + E_{cu}t_{cu}$$
$$x_{2c} = \frac{E_{cu}t_{cu}{}^2 - E_{lcp}t_{lcp}{}^2}{2S}$$
$$H_{33} = \frac{1}{3}\left[E_{lcp}\left[\left(x_{2c} - t_{lcp}\right)^3 - x_{2c}{}^3\right] - E_{cu}\left[(x_{2c} + t_{cu})^3 - x_{2c}{}^3\right]\right] \quad (2)$$

By analyzing the derived equations, it can be seen that the main drivers in the peak stress within the interconnect are the thickness of the constituting layers, and the length of the horizontal member L'. To minimize the problem, thickness should be minimized and L' should be maximized. For a circular arc, the aspect ratio of L/L' is equal to 1, therefore an elliptical arc with aspect ratio less than 1 would be preferable. Knowledge of these

trends is very useful to drive the design and will be used to fine tune the specific values given the geometric constraints of the problem.

2.2.2 Numerical Estimation of Stress Distribution

The above analytical representation offers good insight on the magnitude and location of peak stresses in the proposed geometry, however a more detailed understanding of the complete stress distribution within the spring is desired. For such purposes, a finite element model was constructed using COMSOL. Both a 2D plane strain model and a 3D solid model were constructed using a layered cross-section of Copper and LCP as per the real application. A fixed boundary condition was imposed at the connection point with the post and a separate body was modeled for the antenna aperture. Contacts were defined between the two bodies and an applied vertical displacement was imposed on the aperture, equal to the gap between the two bodies plus the desired combination of preload and cyclic load, which in a typical application is 0.008 inches combined and therefore the value used in the simulation. Material properties were entered as those of pure copper and Rogers Ultralam 3850 LCP. A static deflection analysis was performed and the equivalent Von-Mises stresses were computed for both the cross-section of the entire layer stackup and the outer face of the copper layer. The purpose of this analysis is to compare the peak Von Mises stress experienced in each layer of the interconnect cross-section and to the fatigue curve of the respective material to determine an estimate of the number of cycles to failure that can be endured by the geometry. Given the materials being used, none of them exhibit an endurance limit type behavior so a specific number of cycles to failure can be quoted based on the material that will experience the earliest failure. From the 2D model, the stress distribution along the cross-section of the spring is given in Figure 5.

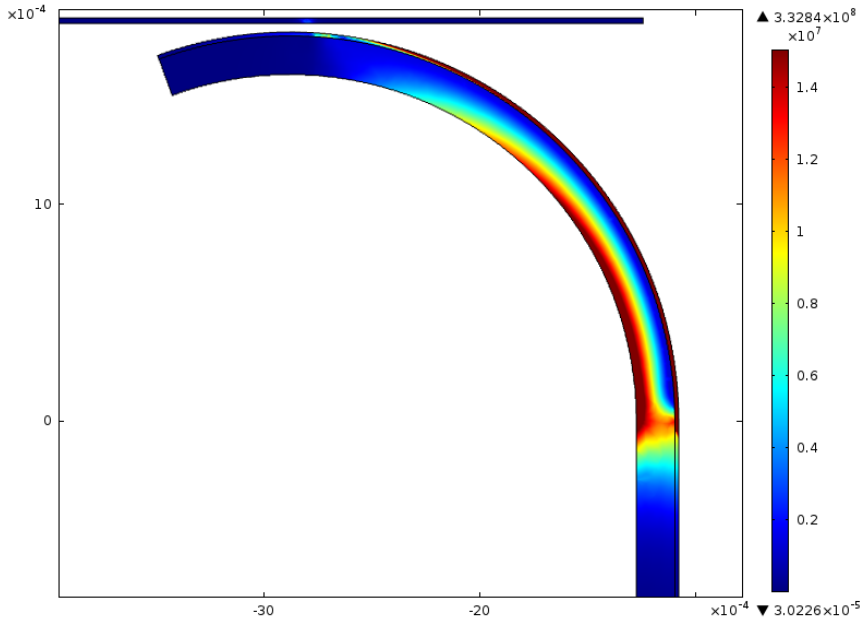

Figure 5: 2D Von Mises Stress Distribution in 90° Arc Connector Cross Section due to 8 mil Total Applied Displacement

It can be seen that the peak stress location matches the analytical prediction, being located at the root of the model, close to the attachment point to the post. In addition, the FEA model also includes the contributions from the shear stress, which is a significant component due to the loading condition and is captured in the equivalent Von Mises stresses, accounting for the asymmetry in the distribution. While apparently the maximum stresses would all allow to meet the goal of 10^7 cycles in all layers, a stress concentration is present in the copper layer close at the boundary with the attachment point that requires further investigation. The full 3D model was therefore run, and visualization was selected to isolate the copper layer. Results for the outermost surface of the copper layer can be seen in Figure 6.

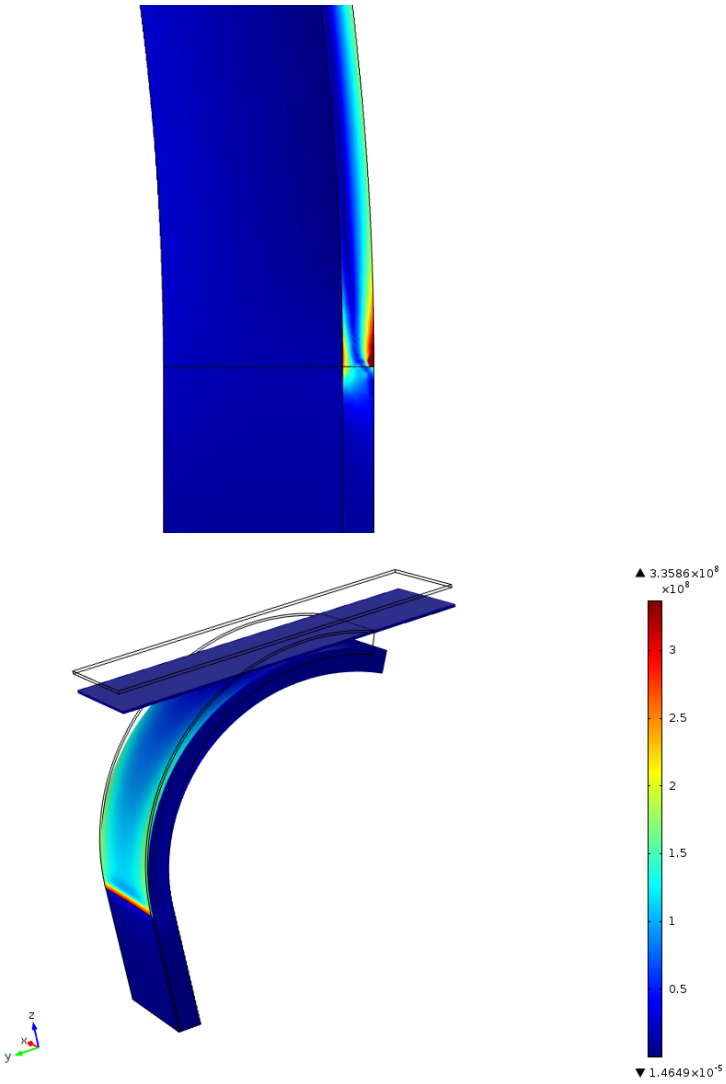

Figure 6: 3D Von Mises Stress Distribution in 90° Arc Connector Copper layer (Right) and Side View Zoom (Right) due to 8 mil Total Applied Displacement

A stress concentration factor of 3 compared to the peak Von Mises stress in the connector was observed at the junction with the attachment point in the copper layer. This concentration, of magnitude 350 MPa, would significantly reduce the fatigue life of the interconnect, and is unacceptably close to the yield strength for copper under certain manufacturing processes. The stress concentration was not predicted in the analytical model as a root fixture point was assumed, while in reality the configuration is fixed at the side of the geometry. Analyzing the individual stress components that make up the equivalent Von Mises stresses we see that the axial stress is actually coherent with the

analytical prediction, but there are transverse normal stress and in plane shear stress contributions close to the attachment point that are not accounted for in the analytical derivation. While this concentration can be reduced by numerically smoothing the boundary condition, using Roark's formulas for stress [14], it would still cause a significantly reduced fatigue life. This loading configuration causes a shear force to be applied at the attachment point, raising the issue of potential solder failure, yet another failure mode which has to be accounted for. While this particular solution is disadvantageous, the idea of a circular arc to describe the spring geometry can still be used to its full potential and allows for smooth stress distribution, but a new solution must be found that eliminates shear at the attachment points, and shifts the peak stress away from the mounting points.

2.3 Semicircular Spring Design

2.3.1 Analytical Estimation of Stress Distribution

As was seen in the previous section, the pure bending approximation was not appropriate for a 90° circle arc connector, as the shear and transverse contributions due to the loading condition and attachment point were significant. However, this approximation would be valid if the load were applied along a line that contained the mounting location, as would be the case for a semicircular simply supported curved beam with applied axial end load, as shown in Figure 7. Furthermore, the maximum bending moment for this geometry and load configuration is located at the midpoint of the arc, resulting in peak stresses that are far away from the mounting points of the spring, which is advantageous in our case.

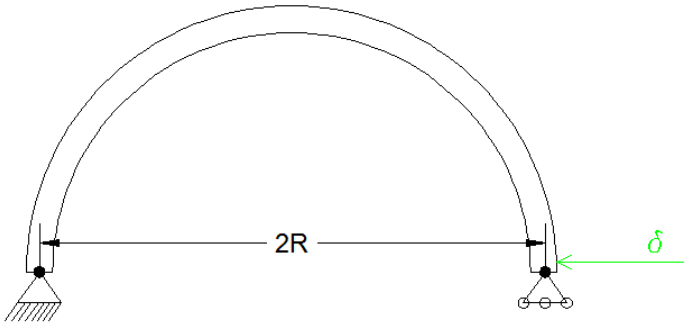

Figure 7: Simply Supported Curved Beam Model with Applied Axial End Load

Such a geometry can be analyzed analytically to derive the stress distribution and peak stress magnitude as per the previous design, and it is expected that the shear contribution will not be significant, at least in the two-dimensional case. Unfortunately such a configuration would require mounting at the bottom of the post, as opposed to the solder pads on the side. This is not possible due to manufacturing constraints, but the design can be refined at a later point to incorporate the required features for production. A preliminary analysis was carried out in the same manner as the original 90° concept to characterize the behavior of this geometry under the proposed loading condition.

Peak stresses were solved for using Euler-Bernoulli curved beam theory assuming pure bending, beginning with analyzing an infinitesimal segment of the beam as shown in Figure 8.

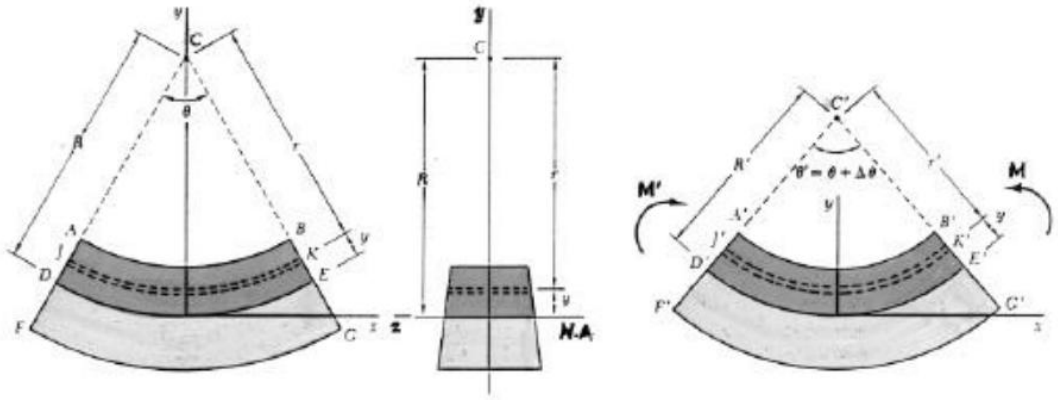

Figure 8: Infinitesimal Curved Beam Section with Geometry and Applied Moments Labeled

The above figure assumes a bending moment applied that causes a change in radius and a change in angle Δθ. Using the definition of strain and letting δ be the elongation of an arbitrary arc length at distance y from the neutral axis, we can express the axial strain as follows:

$$\varepsilon_x = \frac{\delta}{r\theta} = -\frac{y\Delta\theta}{r\theta} = -\frac{\Delta\theta}{\theta}\frac{y}{R-y} \qquad (3)$$

By applying Hooke's Law to equation 3, we can derive the normal stress distribution in the beam as:

$$\sigma^x = E\varepsilon_x = -\frac{E\Delta\theta}{\theta}\frac{y}{R-y} = -\frac{E\Delta\theta}{\theta}\frac{R-r}{r} \qquad (4)$$

By analyzing equation 4 above, a clear dependence on the angle θ can be seen. The angle θ can be defined as the arc swept by the curved beam, with θ = 0° being the point of load application at the roller support and θ = 180° being the opposite pin support, in our case of a semi-circular beam. Taking the derivative of the stress distribution and setting it equal to zero will yield the location of peak stress, which corresponds to θ = 90°, location which is shown in Figure 9 for the proposed semicircular interconnect geometry.

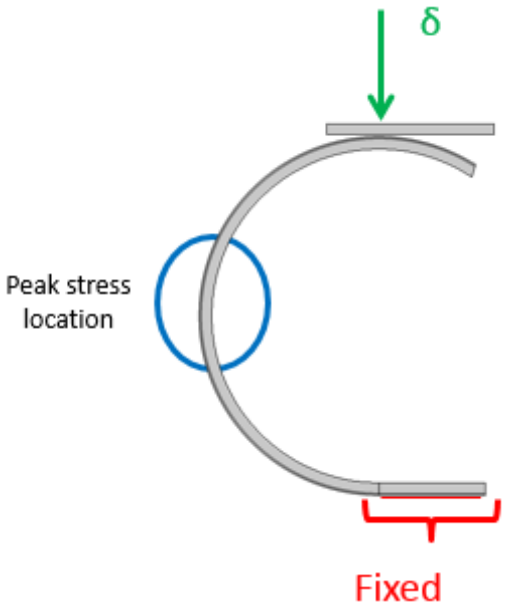

Figure 9: Analytical Peak Stress Location of Proposed Semicircular Spring Design

While the location prediction from our results so far are true for any cross-section composition, it is impossible to compute the magnitude of the peak normal stress as equation 4 assumes uniform cross section, while the copper-clad LCP being used has cross section as shown in Figure 10.

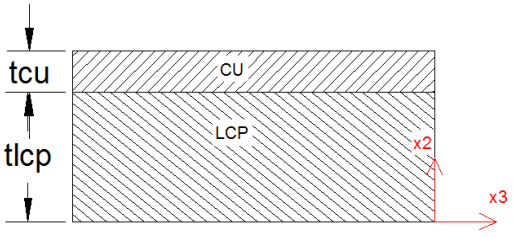

Figure 10: Cross Section Composition for Copper-Clad LCP

Carrying out the derivation for the asymmetric composite cross-section, rewriting the change in angle in terms of the applied displacement, and setting the first differential with

respect to θ equal to zero to identify the peak value, the following dependence is identified:

$$\sigma_{max}{}^{cu}(NotSymCS) \propto \frac{E_{cu}\delta}{2R'^2} \frac{E_{cu}t_{cu}{}^2+E_{lcp}t_{lcp}{}^2+2E_{lcp}t_{lcp}t_{cu}}{E_{cu}t_{cu}+E_{lcp}t_{lcp}} \quad (5)$$

In the above equation, E represents the modulus of elasticity of the subscripted material, t represents the thickness of the subscripted layer as labeled in Figure 10, δ is the applied displacement, and R' is the inner radius of the interconnect. By analyzing the driving factors in the peak stress magnitude, it can be seen that the thickness must be minimized and the radius must be maximized where possible. The radius is dictated by the spacing between the post and the radiating surface, while the thickness is fixed for the supplied copper-clad Rogers 3850 LCP sheet but can be varied for any applied plating, which are necessary for environmental resistance and will be analyzed in a later section. It is to be noted that the semicircular springs proposed are to be concave out, with the radius extending towards the center of the post due to space constraints imposed by the spacing between posts in the final patterned configuration which compose the entire feed card structure. The deformed configuration must carefully be analyzed to ensure that the chosen radius dimension does not cause interference amongst the springs under loading.

2.3.2 Numerical Estimation of Stress Distribution

In order to accurately analyze the stress distribution, confirm analytical predictions and observe the final deformed shape, a finite elements simulation was carried out in COMSOL in a similar manner to the original right-angle design. A semicircular arc was drafted with composite cross-section including both LCP and copper layers, with a straight section at the end. A fixed boundary condition was applied to this

straight section, simulating attachment to the bottom of the post, while the radiating surface was modeled as a separate body and contacts were defined between the two. Contacts were modeled with sliding friction as the gold-to-gold contacts in the real interconnect provide significant friction which cannot be neglected. Vertical displacement was applied to the radiating surface of magnitude equal to the spacing between the two bodies plus the sum of preload and cyclic load equal to 0.008 inches. The solution was computed by performing a static analysis with nonlinear deformations, initially under a 2D plane stress assumption and later in a full 3D solid model. The 2D simulation resulted in an equivalent Von Mises stress distribution in the copper layer versus curvilinear co-ordinate as shown in Figure 11.

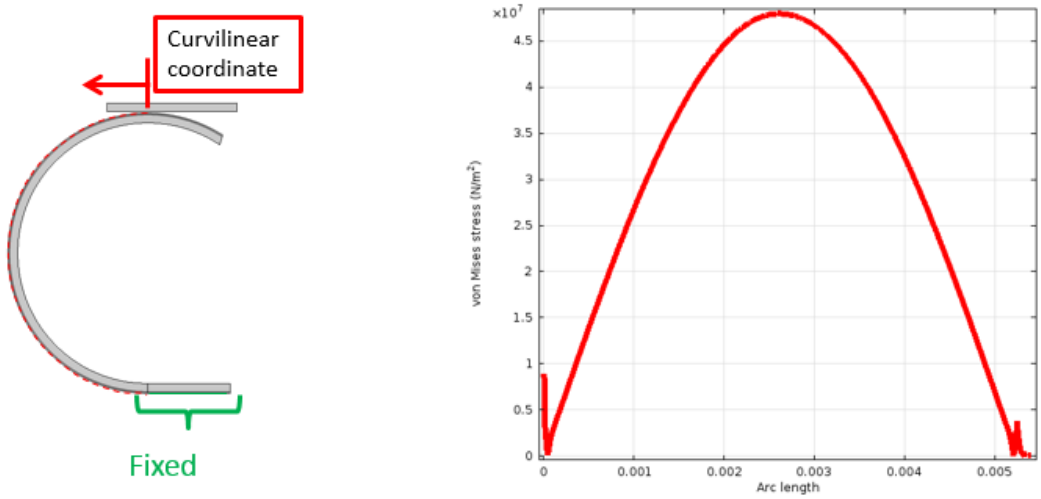

Figure 11: Von Mises Stress Distribution vs. Curvilinear Co-Ordinate in the Copper Layer for 2D Plane Stress Semicircular Interconnect Model due to 8 mil Total Applied Displacement

The computed distribution confirms the peak stress location predicted by the analytical model and shows no stress concentrations, yielding significantly lower peak stress magnitude of 50 MPa compared to the 350 Mpa in the previous design's region of stress concentration. The deformed configuration is shown in Figure 12 and, given the spacing between springs, gives no cause for concern of interference between springs under load as deformation actually occurs away from the center of the post.

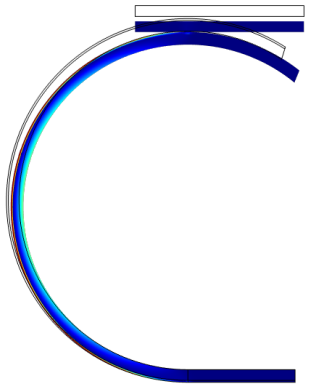

Figure 12: Deformed Shape (shaded) Superimposed on Undeformed Shape (outline) of Semicircular Interconnect Under 8 mil Total Applied Displacement

A final verification was made by running the full 3D model, to observe the presence of any out of plane effects that cannot be captured in the analytical beam model or the plane stress numerical model. Under the same loading conditions, the 3D Von Mises stress distribution is shown in Figure 13.

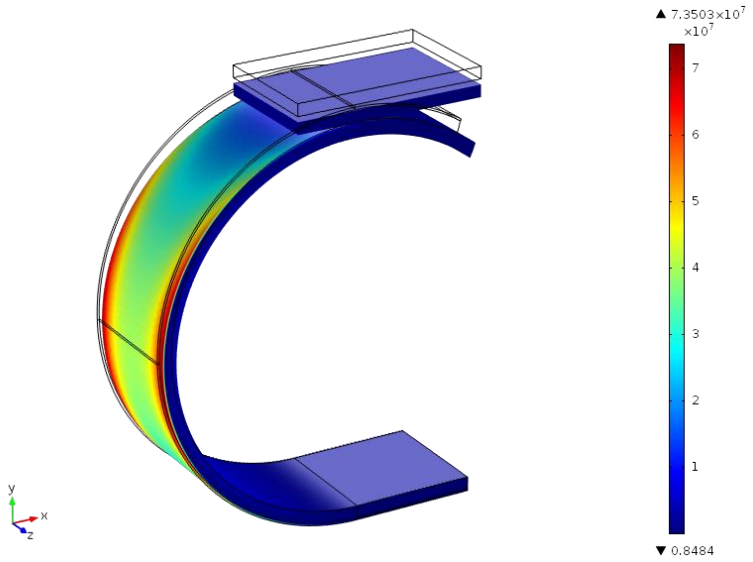

Figure 13: 3D Von Mises Stress Distribution in Semicircular Connector Under 8 mil Total Applied Displacement

It can be seen that a stress concentration of 1.4 is present at the edges of the connector, an out of plane effect that was not predicted by Euler-Bernoulli beam theory and that cannot be captured under the plane stress assumption. The stress distribution in the X-Y plane of symmetry of the connector corresponds to the 2D model prediction. While the resulting peak stress of 70 MPa is still significantly lower than the peak stress in the previous configuration, and meets the design requirements of 10^7 cycles based on the fatigue curve of rolled copper (Between 97 and 127 MPa as tested for thin strips, based on manufacturing process) it is of interest to understand the causes of this stress concentration. In their analysis of the stress distribution in elliptical beams with applied tip loads, Velazquez and Kosmatka [15] observe the presence of through thickness shear stresses and tangential stresses in the solution to the bi-harmonic equation in elliptical co-ordinates after deriving the distribution using a continuum mechanics approach. These terms would not be captured in an Euler-Bernoulli solution as transverse shear is neglected, but will appear in the finite element solution as components to the equivalent Von-Mises stresses.

2.4 Trade Study: Elliptical Spring with Varying Aspect Ratio

The conclusions reached by Velazquez and Kosmatka in the study of elliptical beams prompted the question of how an aspect ratio different from 1 would affect the stress distribution in our spring design. For this purpose, two elliptical geometries were modeled: one with an aspect ratio of 2 and one with an aspect ratio of 0.5. As Velazquez and Kosmatka already provide a thorough derivation of the stress distribution from continuum mechanics, an analytical solution was not derived and the new geometries were analyzed directly using a COMSOL finite element model. Spring cross section was unchanged, maintaining a 4 mil LCP base layer with ½ oz. rolled copper cladding. Boundary conditions were also maintained from the circular model, with a fixed end to

represent mounting to the bottom of the post and a contact set between the spring geometry and the radiating surface, to which a displacement was applied equal to the spacing between the two bodies plus 8 mils. A nonlinear static analysis was performed. Figure 14 shows the 2D Von Mises stress distribution in the Copper layer versus curvilinear co-ordinate for an aspect ratio of 2. It must be clarified that in defining aspect ratio, the separation between post and radiating surface remains unchanged and equal to the radius of the original semicircular design. Therefore, an aspect ratio of 2 will result in an ellipse with a semi-major axis of 2R and a semi-minor axis of R, while an aspect ratio of 0.5 will result in an ellipse with semi-major axis of R and a semi-minor axis of R/2. What is being varied is the protrusion of the spring in horizontal space while maintaining a constant vertical dimension to join the two boards which are required to maintain fixed relative vertical spacing.

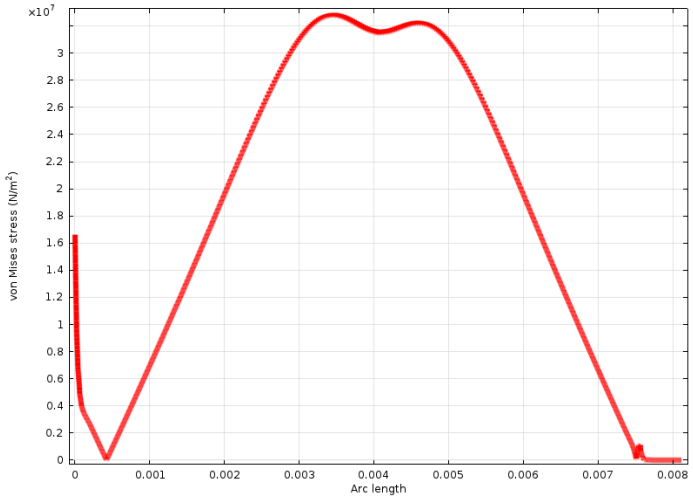

Figure 14: Von Mises Stress Distribution vs. Curvilinear Co-Ordinate in the Copper Layer for 2D Plane Stress Interconnect with Aspect Ratio of 2 due to 8 mil Total Applied Displacement

It can be seen that the stress distribution maintains its symmetry although peak stress location is moved from $\theta = 90°$. The magnitude of the peak Von Mises stress in the Copper layer is significantly lower than the semicircular connector with an aspect ratio of 1, showing a maximum of 37 MPa versus 50 MPa in the semicircular model. In contrast,

Figure 15 shows the 2D Von Mises stress distribution in the Copper layer versus curvilinear co-ordinate for an aspect ratio of 0.5.

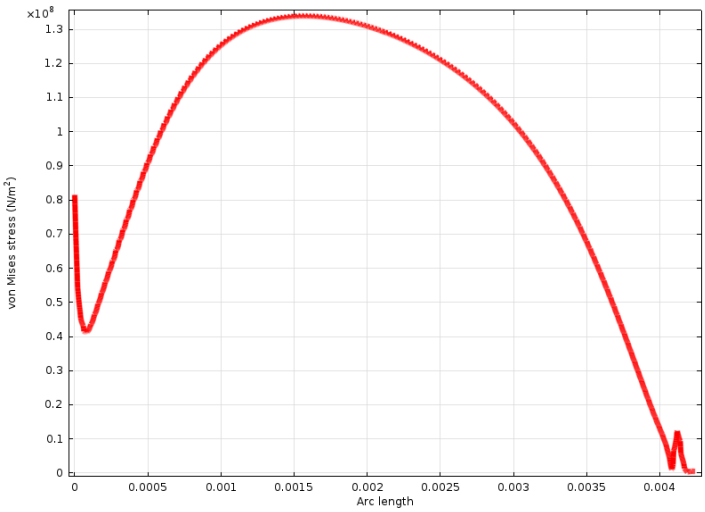

Figure 15: Von Mises Stress Distribution vs. Curvilinear Co-Ordinate in the Copper Layer for 2D Plane Stress Interconnect with Aspect Ratio of 2 due to 8 mil Total Applied Displacement

The most obvious observation is that the stress distribution is no longer symmetric about the curvilinear co-ordinate, meaning the deformation of the connector is not symmetric. Peak stress location has also shifted from $\theta = 90°$ to a point closer to the attachment point with the post. Another interesting phenomenon of reducing the aspect ratio below 1 is also that the magnitude of the peak Von Mises stress in the copper layer has increased from 50 MPa in the semicircular case to 135 MPa. Figure 16 summarizes the effect of varying the spring aspect ratio on the peak Von Mises stress magnitude in the Copper layer. The open circles represent the computed data points from COMSOL simulations, while the solid line is a quadratic interpolation that was performed to extract a general trend. It is unsure whether the peak Von Mises stresses flatten out after an aspect ratio of 2 or increase back, as higher values were not tested and an extrapolation was not performed as it would be inconclusive in determining the actual trend.

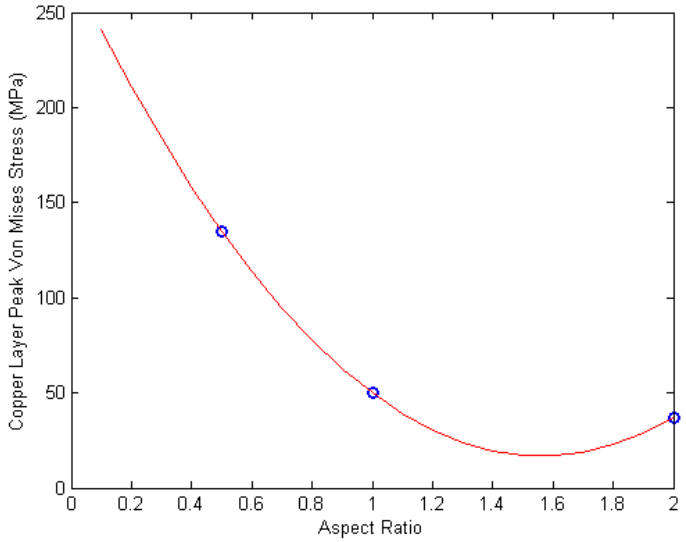

Figure 16: Variation of Peak Von Mises Stresses in Copper Layer with Ellipse Aspect Ratio with Quadratic Interpolation

All elliptical geometries exhibit the same stress concentration factor of 1.4 at the edges when a full 3D simulation is run due to the through-thickness shear and tangential stress components that were not captured in the 2D plane stress simulation. Results of the 3D analysis in the Copper Layer are shown in Figure 17 and 18.

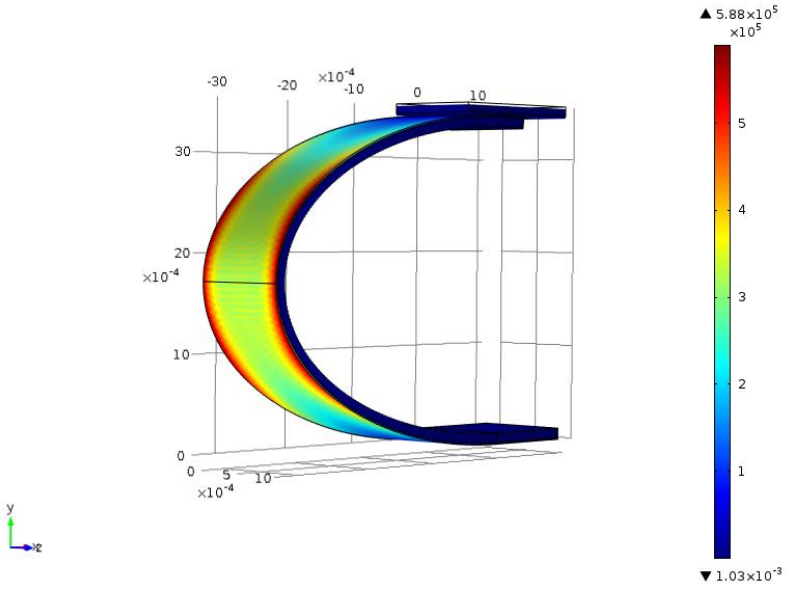

Figure 17: 3D Von Mises Stress Distribution in Interconnect with Aspect Ratio of 2 Under 8 mil Total Applied Displacement

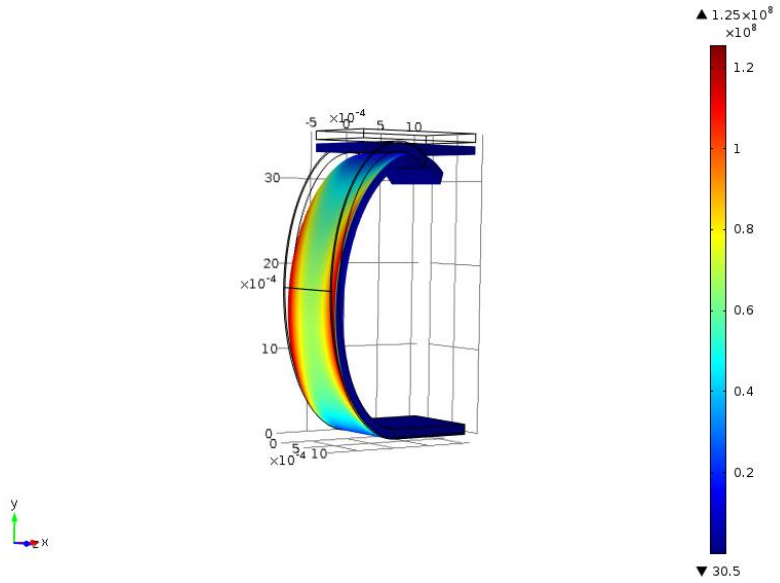

Figure 18: 3D Von Mises Stress Distribution in Interconnect with Aspect Ratio of 0.5 Under 8 mil Total Applied Displacement

Based on this trade study, for the design of a bottom mounted orthogonal interconnect it is desirable to utilize an elliptical spring with aspect ratio between 1 and 2, as larger elliptical aspect ratios provide advantages in the form of lower peak Von Mises stresses in the Copper layer compared to a purely semicircular design. Unfortunately, due to the geometry constraints of this specific application, an elliptical solution would not be possible. In the current concave-out geometry, increasing the aspect ratio will cause interference between the springs, while switching to a concave-in configuration would require a greater spacing between posts than is currently possible on the current RF circuit card for which this interconnect is required. However, for future orthogonal interconnect applications, this remains an important results to guide the design of a future appliance with different geometric constraints.

2.5 Optimization Studies in Confirmation of Analytical Results

A final verification of the results obtained as far as defining driving parameters in determining the peak stress magnitude in the interconnect spring was performed using basic numerical optimization tools. The optimization problem was implemented in MATLAB beginning with the circular stress distribution for the metalized LCP as

expressed in equation 5 as the function to minimize. However, the design space is subject to several constraints, mainly with regards to the physical size of the spring relative to its surrounding features in the feed card. It was therefore decided to utilize a constrained minimization through the *fmincon* function where constraints were set on the three variables: radius, LCP thickness, and Copper thickness. A trust region reflective algorithm was used for the minimization. The radius was constrained from 0.001 inches to the spacing between the feed card and radiating surface, and the cross-sectional layer thicknesses were constrained from 0.001 to 0.01 inches. The results of the computation, initialized with values in the middle of the supplied ranges, confirmed original predictions, with the optimal combination being the largest possible radius and the smallest possible layer thicknesses. The largest possible radius is in fact the spacing between the two cards being interconnected, and while the layer thicknesses of LCP and Copper are constrained by the chosen material, this result will be useful in the following section when platings are selected for environmental protection of the Copper layer.

2.6 Design Towards Manufacturing: Effect of Plating on Stress Distribution

For the purpose of environmental survivability, with particular regards to corrosion resistance, an exposed bare copper finish is unadvisable as oxidation will occur over time, greatly reducing the RF performance. Keeping with the current RF appliance state of the art, it is desirable to electroplate the springs with a Nickel-Gold plating. Gold is naturally corrosion resistant and also provides good wear protection when relative motion between the post and the radiating surface occurs. However, if a Gold plating were to be applied directly onto the Copper, diffusion of ions would occur between the two layers. In order to avoid this phenomenon, a layer of Nickel is placed in between to isolate the two layers and ensure longevity of the plating. Due to the cross-sectional thickness dependency of peak stresses in the semicircular interconnect, the plating layers must be incorporated into the COMSOL finite element model to ensure that the resulting

peak stress in each layer remains below the fatigue strength of the respective material at 10^7 cycles. A diagram of the cross-sectional layer stackup for a complete LCP interconnect is shown in Figure 19.

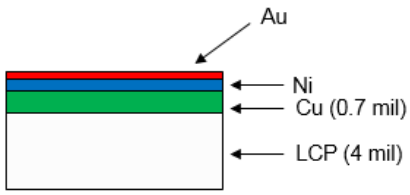

Figure 19: Stackup of Layers Composing the LCP Interconnect Cross-Section

Harris circuit designers recommended a minimum of 250 µIn of Nickel in order to properly insulate the Copper layer and avoid ionic diffusion. Since this is the minimum required thickness and cross-sectional thickness must be minimized per our stress distribution equation, 250 µIn of Nickel will be used and were implemented in the FEA model. The model was run performing the same static analysis that was earlier performed on the bare copper interconnect, with a total tip displacement of 8 mils applied via the mating board and the defined contacts. The Von Mises stress distribution versus curvilinear co-ordinate of the 2D model for two different Gold thicknesses (50 and 100 µIn) is shown in Figure 20.

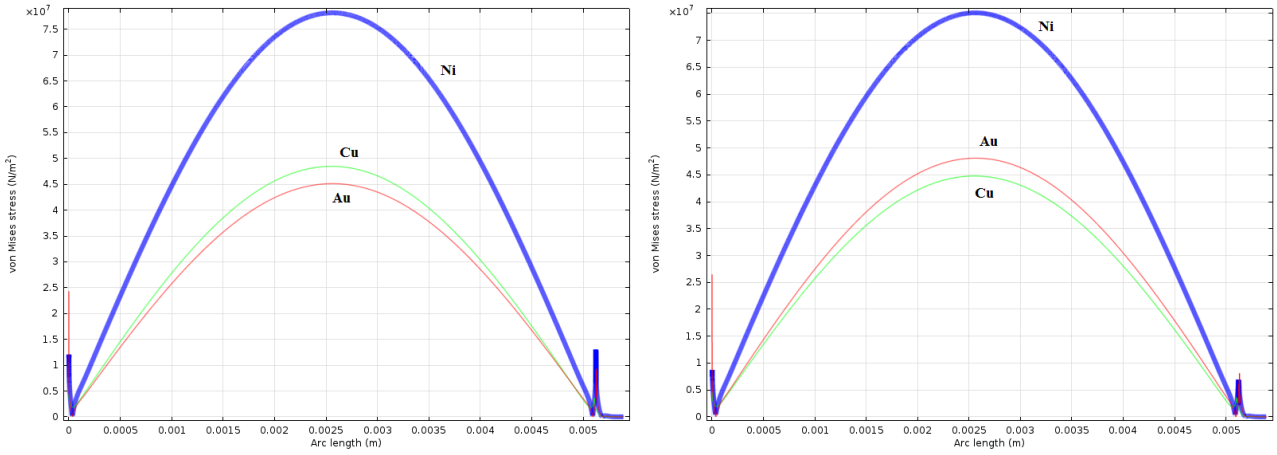

Figure 20: Von Mises Stress Distribution vs Curvilinear Co-Ordinate from 2D FEA Simulation for 50 µIn Au (Left) and 100 µIn Au (Right) over 250 µIn Ni

The 2D results show a strong dependency of peak stresses on the gold plating thickness. As can be expected, the Nickel layer incurs in the highest peak stress as it has the highest modulus of the two. However, even though an increase in peak stress is expected from the increase in overall cross-sectional thickness, it does not occur linearly in all layers. Nickel peak stresses actually decrease from 80 MPa to 75 MPa when the Gold thickness is doubled from 50 to 100 µIn. The magnitude of peak equivalent stresses in the Gold and Copper layer switch places as the Gold thickness is doubled, moving from 45 MPa to 48 MPa in the Gold and from 48 MPa to 45 MPa in the Copper. It can therefore be concluded that an increase in thickness of an individual metal layer in the cross-section causes an increase in peak stress in that layer, which does not translate automatically to the other layers.

For reference, the fatigue strength at 10^7 cycles for the various layers is:

- Copper: 95 – 127 MPa
- Nickel: 250 – 345 MPa
- Gold: 46 MPa

The ranges are obtained from raw material manufacturers and are based on different treatment processes to reach the final product. Peak equivalent stresses are well within the fatigue strength for Copper and Nickel, while they are at the limit in the Gold layer. For this reason, it was decided to plate the interconnect with only 50 µIn of Gold as it would result in the lowest Gold peak stresses, at the expense of the other layers which have at least factor of 2 margin on their worst case fatigue strength at 10^7 cycles. Harris subject matter experts agreed that it was a sufficient thickness to ensure wear resistance during relative motion, as the resulting Gold-to-Gold contact is very high friction and wear of the two plating layers is to be expected.

2.7 Design Refinement for Side Mounting to the Post

Recalling from the original requirements for this design, the interconnect spring must be mounted onto solder pads positioned on the side of the post and make contact with an orthogonal radiating surface. The initial 90° arc design that allowed for a smooth transition between the two planes was unacceptable due to stress concentrations at the boundary condition interface where the spring mounts to the post from shear loading, while the semicircular geometry currently pursued would require theoretical mounting to the bottom of the post, which is impossible from a manufacturing point of view. As the semicircular configuration has significant advantages in the stress distribution and peak values, it must be adapted to allow for side mounting without incurring into the problems experienced by the initial design. An initial solution proposed involved a 90° elbow joint at the top of the semicircular connector that would allow side mounting to the post and connect to the existing curved geometry, maintaining a single smooth sweep for the purpose of eliminating any stress discontinuities. A rendering of the mounting solution is shown in Figure 21, with the straight vertical section to be used for mounting.

Figure 21: Rendering of the Modified Spring Design for Side Mounting

A few immediate problems are immediately evident in observing this geometry. The primary issue is that, due to the requirement to maintain a fixed spacing between the tip of the post and the radiating surface, the radius of the connector must be decreased to fit the elbow joint into the fixed opening. The redesigned radius is roughly 2/3 of the

original radius dimension analyzed in the semicircular design. Due to the radius dependency on the peak Von Mises stress magnitude, it is therefore expected that this magnitude will increase in all layers, while maintaining the same location. Furthermore, the elbow joint itself has a very small radius of roughly 1/3 the original semicircular radius, which could potentially incur in very high stress concentrations following the original analysis on a 90° circular arc connector.

To verify these concerns and quantify the changes, the redesigned geometry was modeled in COMSOL with full plating layers in the cross section and the appropriate boundary conditions. These included fixing the straight vertical surface to the post, defining contacts between the spring and the radiating surface body, and applying a displacement to the radiating surface equal to the gap between the two plus 8 mils. The 2D Von Mises stress distribution after nonlinear static analysis can be seen in Figure 22.

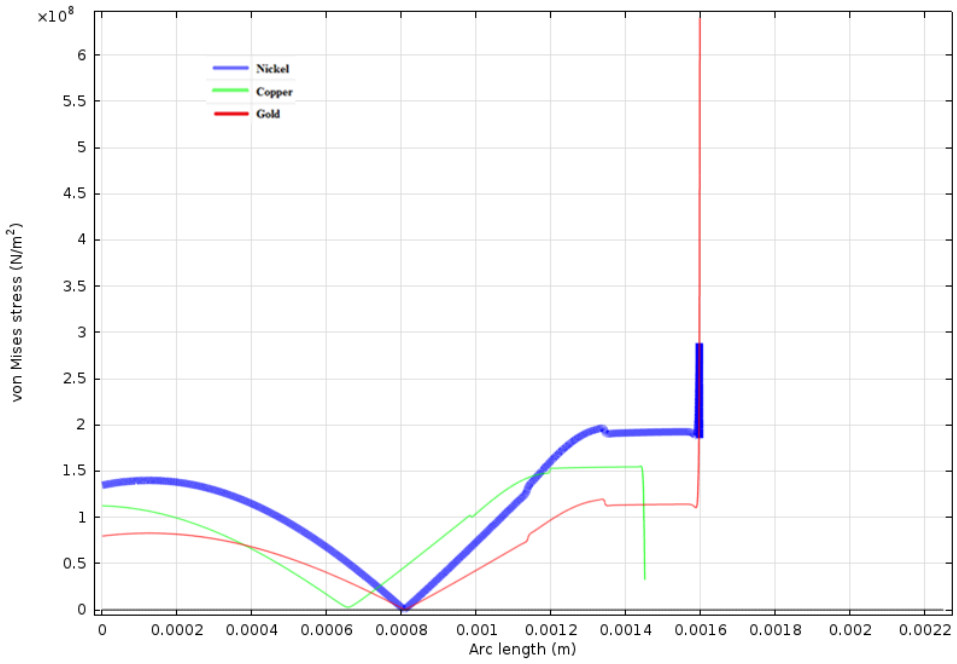

Figure 22: Von Mises Stress Distribution vs. Curvilinear Co-Ordinate for 2D Plane Stress Revised Interconnect Model due to 8 mil Total Applied Displacement

To reduce computational time, since the stress distribution in the semicircular interconnect design was symmetric, computation was performed only from the midpoint

of the large radius ($\theta = 90°$, which corresponds to the origin of the x-axis in Figure 22) to the fixture point on the post. Two effects are evident from the computed distribution. The peak Von Mises stresses in the Copper, Nickel, and Gold layer for the large radius increase to 110 MPa, 145 MPa, and 80 MPa respectively, which when compared to the fatigue strengths at 10^7 cycles quoted in the previous section puts the Gold layer beyond its fatigue strength, the Copper layer at its limit and the Nickel layer still well within limits. Assuming the stress concentration factor of 1.4 is still present in the 3D case, this will allow the connector to still potentially reach 10^7 cycles with expectation of failure in the Gold layer. It will be unclear until testing whether failure of the Gold layer will compromise the operation of the interconnect spring. The Gold layer is still expected to last at least 10^6 cycles, providing a good starting point for the design even in the worst case scenario, as design refinements such as selective plating of only the areas where corrosion resistance is vital will significantly improve the fatigue life of the interconnect. More alarmingly though, the stress distribution in the small elbow joint is highly unfavorable, with peak stresses in the Copper, Nickel, and Gold layers of 150 MPa, 105 MPa, and 200 MPa respectively, which compromises survivability of the entire interconnect to the number of cycles required. Furthermore, a stress concentration at the boundary condition interface between free and fixed is present as was in the original design. While structural analysts at Harris agreed that the magnitude of the concentration was more than likely a numerical construct due to the boundary condition discontinuity, the presence of this concentration cannot be ignored, as it points to shearing of the fixture point, and the many other failure modes that could occur such as solder failure. Fortunately, since the straight section protrudes vertically below the tip of the post before the elbow joint defines the curved features of the interconnect, a solution is available that eliminates the stress concentration problem at the attachment point and the high peak stresses in the elbow joint, allowing an acceptable albeit high level of stress concentration in the main radius. A hard stop, composed of a block of dielectric, can be placed on the

tip of the post, which will make contact with the elbow joint under load, limiting its deformation. A diagram of the hard stop setup is shown in Figure 23 for a single spring.

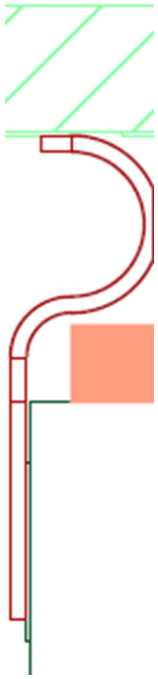

Figure 23: Schematic of Dielectric Hard Stop Incorporation on the Tip of the Post

This hard stop, cut out of ULTEM 1000 dielectric and glued with epoxy onto the tip of the post, serves two primary purposes. First of all, it limits travel of the elbow joint, limiting the magnitude of Von Mises stresses in the joint and eliminating any shearing force on the attachment point. Secondly, it approximates the bottom mounted boundary condition that was analyzed in the first iteration of the semicircular interconnect design, ensuring behavior of the prototype is close to what was modeled, with the exception of the radius dimension. RF simulations were performed and the dielectric block has no effect on the electrical performance of the spring under a typical application.

2.8 Conclusions

Using the lessons learned from previous designs, a list of guiding principles was created for the design of a spring finger type orthogonal interconnect, of which the most important was the avoidance of sharp geometry transitions that create discontinuities and

concentrations in the stress distribution throughout the connector under loading. An initial design was analyzed using a 90° semicircular junction between the two perpendicular planes, but finite element simulations showed a high stress concentration fixture at the boundary condition interface between free and fixed due to shearing of the attachment point which was not taken into account by Euler-Bernoulli theory. A new geometry was proposed using a semicircular geometry which could be approximated by a curved beam in pure bending, eliminating any shearing effects and providing significantly lower peak stresses than the previous design. Peak stress magnitude in this geometry was found to be inversely proportional to the semicircle's radius and directly proportional to the cross-sectional thickness, although finite element simulations incorporating various plating layers on the Copper-clad LCP showed that the increase in stress in a particular layer due to an increase in its thickness do not translate linearly to the remaining layers. In fact peak stress in some of the other layers actually decreased when only one layer's thickness was increased. An ideal combination of plating thicknesses was identified for environmental survivability and to ensure the connector would survive 10^7 cycles, however this design presumed mounting to the tip of the post instead of its sides, which was not feasible from the manufacturing point of view. A redesigned connection point was subsequently proposed using an elbow joint that would allow side mounting, together with a hard stop on the tip of the post to limit deflection of the elbow joint and shearing of the attachment point, ensuring that the design goals in fatigue life would be met.

CHAPTER 3

INTERCONNECT PROTOTYPE MANUFACTURING

3.1 Manufacturing Technique: Introduction to Thermoforming

In order to manufacture a prototype interconnect, two important processes must be defined: a forming process to impart the desired spring geometry to a sheet of copper-clad LCP, and a process to mount the spring fingers onto a post. The thermoplastic properties of LCP were used to achieve the desired geometry through a thermoforming process, in which a sheet of LCP was placed in a mold and vacuum formed after being pre-heated to a desired temperature. Thermoforming of Liquid Crystal Polymers has been investigated by Mogilevsky et. al [16] and is highly process dependent, with specific conditions necessary for each individual polymer blend. Furthermore, the anisotropy created by the strongly directional orientation of fibers within the polymer matrix is maintained after forming, requiring a careful mold design to achieve the desired geometry without affecting material properties of the finished product.

The key to a successful thermoforming is, with a properly designed mold for the application, to pre-heat the LCP to a temperature below its glass transition temperature, at which the matrix will soften but not flow. Vacuum can then be applied to the softened material to form it into the geometry of the mold. Temperature control is vital, as the process requires a high enough temperature where the material will soften sufficiently to be formed, but if the glass transition temperature is exceeded, the matrix material will begin to flow, distorting the geometry of the sheet and randomizing the orientation of fibers. This effect was demonstrated by Sun et. al. during thermoforming trials of thermoplastics locally reinforced with LCP [17]. The glass transition temperature can vary between 150°C and 300°C depending on the polymer blend and manufacturing

technique, so a specific temperature must be dialed in to ensure the required feature resolution without damage to the sheet. In some cases it might be necessary to add additional pressure within the autoclave after pulling vacuum.

3.2 Breadboard Tests and Initial Trials

In order to verify our thermoforming capability, ensuring all feature sizes could be resolved, and to determine the best performing process parameters, a breadboard was designed and manufactured to run trials with LCP samples. The main concerns that were required to be addressed by the breadboard runs were: feature resolution, possible LCP spring-back after forming, interfacial behavior between LCP and copper layers, and the effect of residual thermal stresses on the copper cladding. The breadboard was manufactured from a plate of ¼ inch mild steel in which four 1 inch grooves of increasing diameter were cut with a ball-end mill, performing as the negative half of the mold. The mill was then used to create a 45° chamfer on one of the edges of each groove, to assess the resolution of the process and observe whether smoothing the transition between features has a beneficial effect on the resulting formed geometry. The positive mold was provided by gauge pins of matching diameter that were dropped onto the LCP sheet after it was placed in the negative mold. A diagram of the breadboard with corresponding groove diameters in inches can be seen in Figure 24.

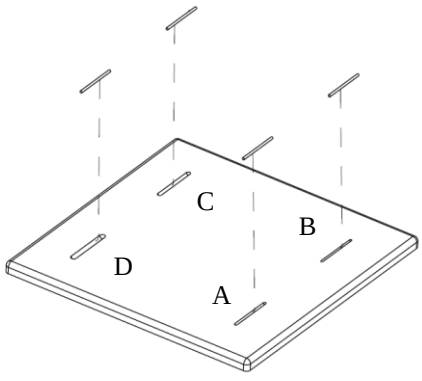

ITEM	DIMENSION
D	.062
C	.046
B	.031
A	.024

Figure 24: Layout and Groove Diameters of Thermoforming Breadboard

It can be noted that the edges of the breadboard are filleted. This is due to the forming process requiring the setup to be placed in a vacuum bag, which cannot allow sharp edges due to the risk of perforation during vacuum operation.

The run was performed with Rogers 3850 copper clad LCP blend that will be used for the spring manufacturing. The LCP strips mounted on the plate with the corresponding gauge pins to provide a positive mold can be seen in Figure 25. The strips were position metallized side down and held in position with Kapton tape and the top two strips have been unmounted after forming.

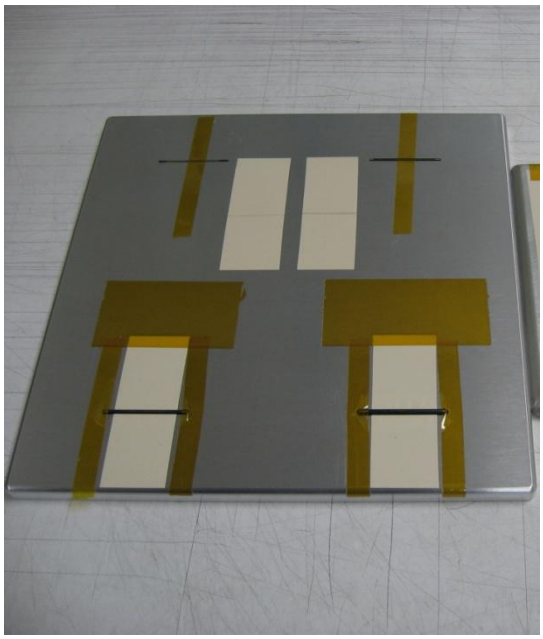

Figure 25: Thermoforming Breadboard and Corresponding Gauge Pins with the Bottom Two LCP Strips Mounted and the Top Two Unmounted After Forming

After the initial run, the settings of which are unfortunately proprietary to Harris and cannot be disclosed, the samples were cast in an epoxy cylindrical mold which acted as a supporting material, and microsectioned to obtain a detailed cross-sectional observation under a microscope. All radii were formed accurately within tolerances, with a slight amount of spring-back observed for the larger diameter grooves leading to a formed radius larger than designed. The results for three of the samples can be seen in Figure 26.

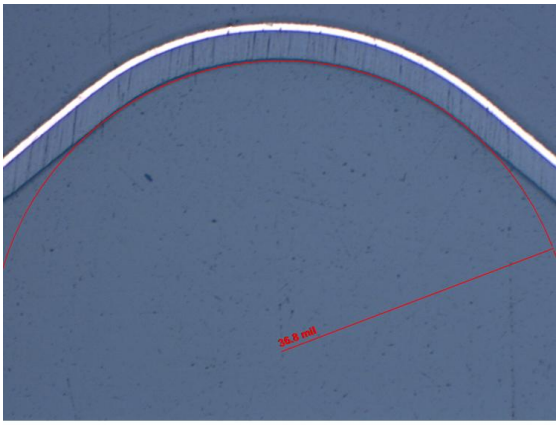

(A)

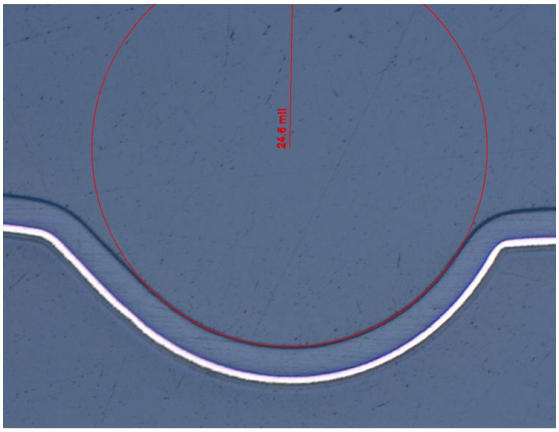

(B)

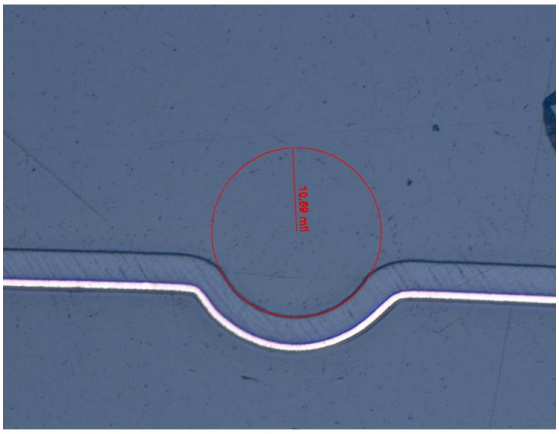

(C)

Figure 26: Microsections and Measured Internal Radius (mils) at 50x Magnification for (A) 63 mil diameter (B) 46 mil diameter (C) 24 mil diameter

The microsections were then analyzed under high magnification to observe the condition of the copper cladding. The metalized layer appeared to be intact, following the contours of the mold accurately without damage. No cracks or delamination with the LCP base

were observed although some compression of the layer in correspondence of the non-chamfered bend lead to a localized thinning in all samples between 4 and 7 microns. The microscope images with marked copper layer thickness in microns can be seen in Figure 27. This demonstrates that a gradual transition must be had between features in the form of a chamfer or fillet to obtain the best possible forming resolution without affecting the constituent layers.

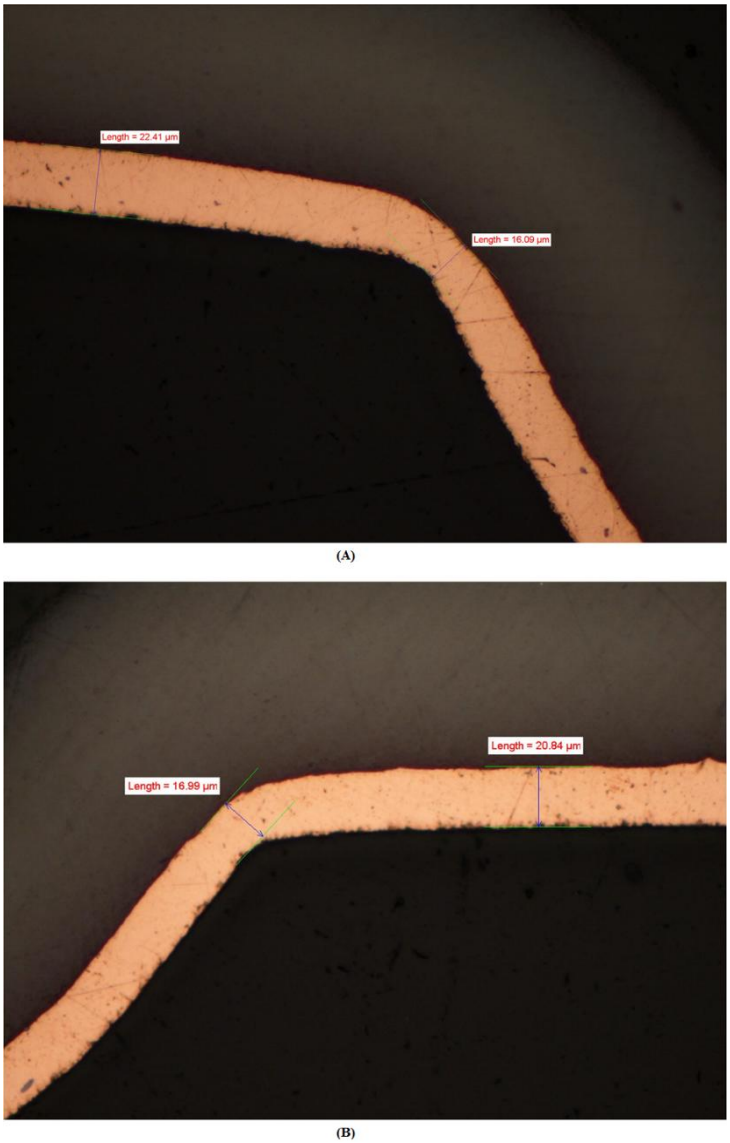

Figure 27: Microsections and Measured Copper Thickness (µm) at 500x Magnification for (A) 46 mil diameter (B) 24 mil diameter

3.3 Tooling Design and Fabrication

With the knowledge gained from the breadboard forming runs, it was then possible to design a set of tooling fixtures to properly thermoform the final spring geometry. Due to the excellent results of the breadboard design, which demonstrated a forming capability down to a radius of 0.01 inches and set a new state of the art benchmark for the process at Harris, it was decided to maintain a two-part mold design using mild steel plates. The negative mold was machined using a Wire EDM from a piece of 2.5 x 1 x ¼ inch steel and contains a groove to impart the spring's larger radius, while a fillet equal to the diameter of the spring's smaller radius was used on the groove's edge to impart the small elbow joint and smooth the transition between the two, as was observed from the initial forming runs. Two alignment pins were designed into the negative for placement of the unformed LCP printed wiring board that would contain the traces for each spring. A rendering and schematic of the negative mold is shown in Figure 28.

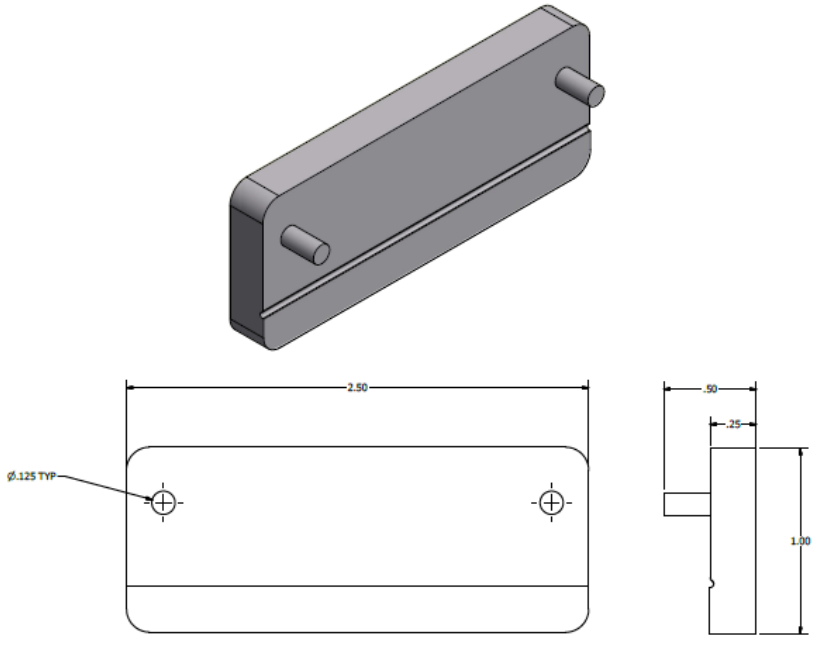

Figure 28: Rendering and Schematic of the Negative LCP Forming Mold

The positive mold was also machined using a Wire EDM out of an analogous steel plate and maintained the same features but now the radii were extruded instead of recessed. Two alignment holes were placed in the piece to correspond with the alignment pins on the negative: a circular and elliptical hole to guarantee proper tolerances and account for thermal expansion in the autoclave, allowing for a clean de-mating after forming. All external edges of both mold halves were filleted to avoid sharp edges that could tear the vacuum bag in the autoclave. The positive mold rendering and schematic is shown in Figure 29. A tolerance to accommodate the strip of 4 mil LCP with ½ oz. copper cladding was incorporated into the fitment between the two mold halves.

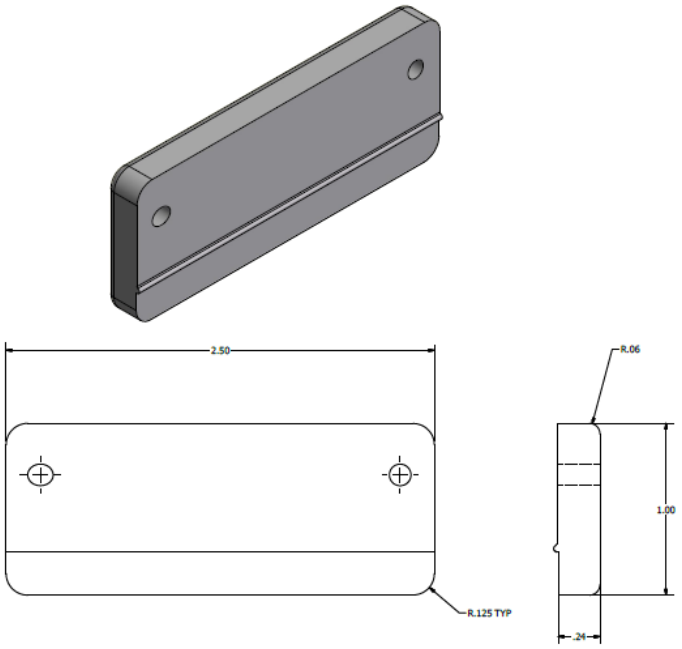

Figure 29: Rendering and Schematic of the Positive LCP Forming Mold

A board layout for the interconnect springs was subsequently required to function with the forming tools as designed. To accelerate the manufacturing process due to the tight schedule demands of the autoclave, the molds were sized to form four interconnects at a time, and a set of three molds was produced. In order to best utilize the surface area of the metalized LCP sheets, sets of four interconnects were mirrored and connected at the tips, resulting in a rectangular PWB with symmetrical copper traces corresponding to

the eight mirrored sets of springs. Alignment holes were placed on the board in correspondence to the holes on the positive mold to allow fitment on the negative mold's alignment pins and also designed to have a circular and an elliptical hole with the required tolerances for de-mating. A schematic of the resultant circuit board layout is shown in Figure 30. Red hatching represents copper metallization while blue hatching represents bare LCP. The specific feature dimensions were omitted due to them being proprietary to Harris.

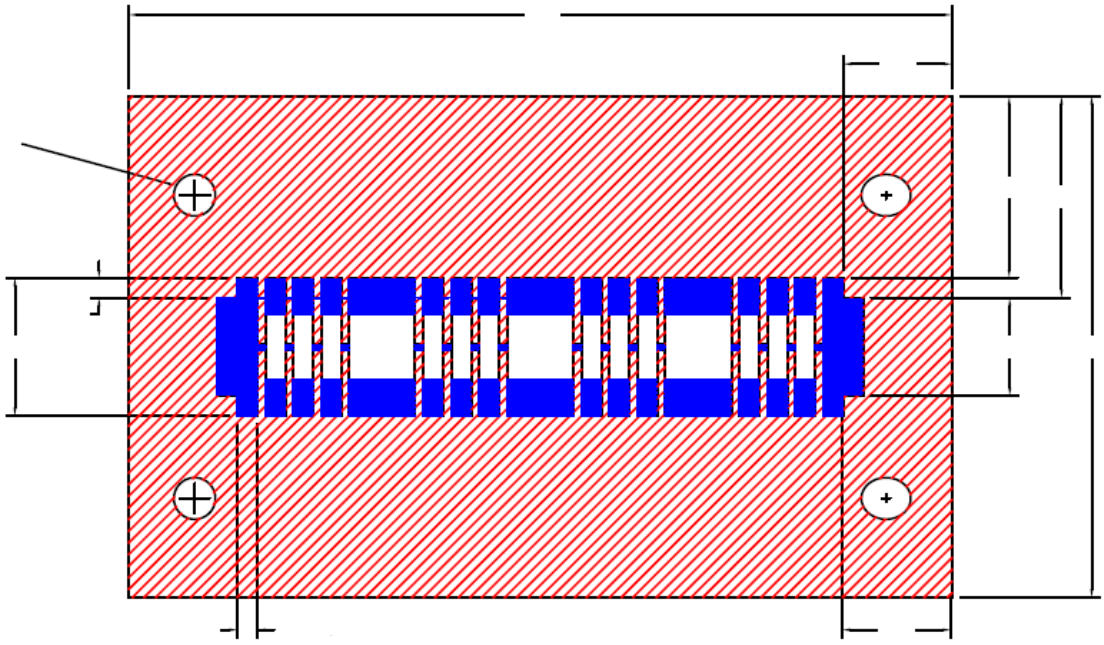

Figure 30: Printed Wiring Board (PWB) Layout for 8 Sets of LCP Springs

It can be noted that the metallization on the board extends well beyond the interconnects. This is to allow for placement of the electrodes required for the electroplating process that will apply the hard Nickel-Gold plating. It was desired to conduct trials with plating both before and after thermoforming, and this layout allows the flexibility to proceed in both orders. To proceed with forming and installation, the board must be manipulated into the correct geometry. It must first be separated in half to allow each half to be inserted in the mold, then separated into the individual interconnect spring sets to be mounted. This was achieved through laser singulation, and a cutting diagram is shown in

Figure 31, where the red lines represent cuts to be made before forming and the green lines representing cuts to be made after forming. Dimensions are once again omitted.

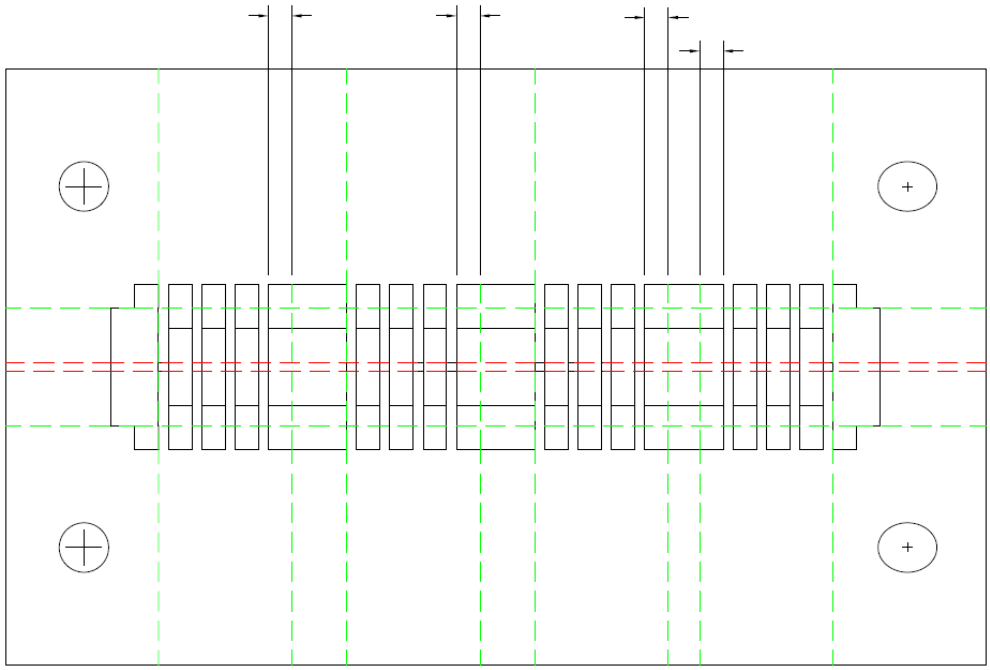

Figure 31: Cutting Diagram for Laser Singulation of Spring PWB

The layout in Figure 30 was used to generate a photoplot, which defines the location of the metallization on the board and is used to guide the chemical etching process used to define the copper artwork. The photoplot is superimposed on a sheet of fully metallized LCP and cured under ultraviolet light to deposit a masking film layer in correspondence of the desired metallization. The board is then inserted into a chemical bath which etches away the copper on any area not covered by the cured film, resulting in the final artwork arrangement. Manufacturing was outsourced to Metro Circuits, a legacy circuit board manufacturer, and the resulting board is shown in Figure 32. A total of 27 boards were ordered based on the maximum amount that could fit on a standard sheet of copper clad Rogers 3850, and half were sent for electroplating before forming, while the other half were formed first and then electroplated.

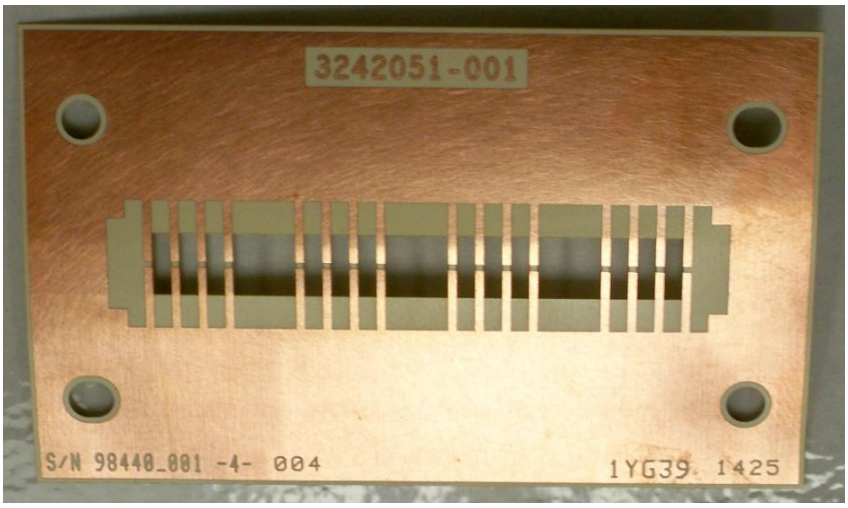

Figure 32: Fabricated PWB for 8 Sets of LCP Springs Before Singulation and Forming

3.4 Spring Thermoforming Results

After the initial separation into two sets of four springs, the first board was placed in the two part mold and thermoformed with the autoclave set at the same parameters as the breadboard runs, which had previously proven successful. The results of the initial run can be seen in Figure 33 for a single spring.

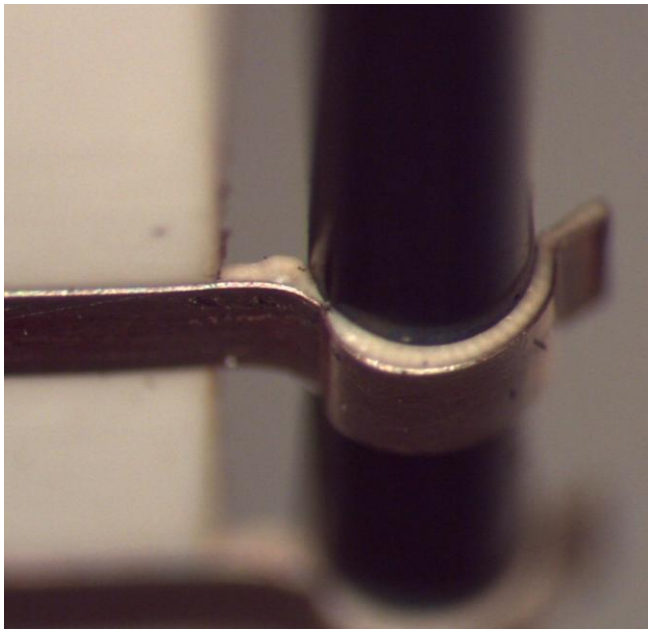

Figure 33: Resulting Formed Shape After First Trial of Spring Forming with Two Part Mold

It can be seen that the results are not acceptable as the base layer is damaged and the geometry is distorted from the original design. The main issue encountered is that the mass of the positive lead the LCP to displace under compression, causing it to delaminate from the copper cladding. Also, the steel plate has a non-negligible thermal mass, causing the temperature of the LCP to locally exceed its glass transition temperature, facilitating flow and delamination. The spring pictured was fused to the positive mold and could not be separated without being destroyed. Furthermore the LCP deformation did not allow the full geometry of the spring to be resolved, as can be noted by the remaining overhang at the tip.

It was therefore obvious from the first run that the tooling required a redesign to account for the observed issues, as well as there being a need to fine tune the autoclave parameters to accommodate the new geometry, which, due to the smaller feature size of the springs, makes it easier to incur in delamination. Since the breadboard setup had provided excellent results, it was decided to adopt a hybrid approach between it and the two part mold design that was tried for spring forming. The negative mold was maintained, replacing the simplified grooved plate of the breadboard, and gauge pins of matching diameter to the spring's large radius. The unformed PWB would be placed on the negative mold through the alignment pins as it had previously, but a simple gauge pin would be fixed on top of the groove as a positive instead of the complete plate. Gauge pins are significantly lighter, their thermal mass can be neglected, and offer adjustability of the tolerance between the internal and external radius of the final geometry. The hybrid setup is rendered in Figure 34. Forming runs were performed varying the gauge pin diameter between 0.028 and 0.030 inches to achieve a varying degree of difference between inner and outer radius and observe the result on the formed geometry.

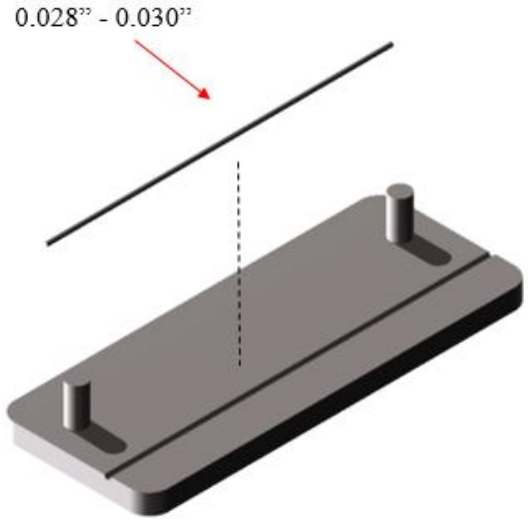

Figure 34: Rendering of the Hybrid Negative Mold with Gauge Pin

A spring formed with the 0.028 inch pin is shown in Figure 35 while a spring formed with the 0.030 inch pin is shown in Figure 36.

Figure 35: LCP Spring Formed With Hybrid Mold Using a 0.028" Gauge Pin

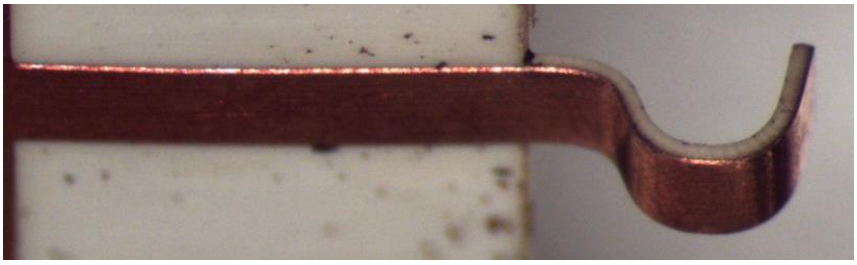

Figure 36: LCP Spring Formed With Hybrid Mold Using a 0.030" Gauge Pin

It can be seen from the images above that a 28 mil diameter pin does not accurately resolve the tip geometry of the spring, as it is not large enough to impart curvature on the

whole spring. Conversely, the 30 mil diameter pin resolves the desired geometry perfectly allowing manufacturing of the designed geometry. There must therefore be no difference in the radius between the groove in the negative mold and the gauge pin to obtain the best resolution in thermoforming. With regards to the autoclave settings, the temperature was lowered slightly relative to the breadboard trials to ensure the LCP was kept below its glass transition temperature for this particular mold setup. Tests performed with previously plated springs showed no difference in results, and both nickel and gold layers formed smoothly without cracking or delamination. No difference in residual thermal stresses was noticed between plated and unplated samples.

3.5 Interconnect Final Assembly

Final assembly of the interconnect on the test fixture was carried out manually by a technician at the Harris Microelectronics Laboratory. The initial step involved bonding a small rectangular PWB on each side of the test fixture's post. Rectangles were cut from a sheet of copper clad Rogers 3850 LCP, forming a single conductive trace over which a solder mask was applied, leaving two exposed pads at the ends. The boards were then floated on a bath of molten tin solder to deposit a solderable metallic layer on the exposed pads. An LCP spring will be attached to one pad, while a lead wire carrying an input signal for the vibration test will be attached on the other. Having pre-assembled solder pads makes the soldering process significantly easier, as the surface just needs to be heated upon application of the spring or wire in order for the solder to temporarily reflow and bond with the additional item. This ensures a cleaner and sturdier solder connection compared to the traditional method of applying molten solder with a soldering iron. A rendering of the masked PWBs is shown in Figure 37. The PWB strips were bonded on each face of the post, for a total of four, using epoxy as the bonding agent. Care was taken to ensure the top of the board was as flush as possible with the tip of the post, and no variation in the height was present amongst the four boards as that would cause a

difference in the height of the springs as they all need to protrude within a 0.001 in tolerance to ensure proper preload during testing.

Figure 37: Rendering of a Single PWB for Mounting of LCP Springs on the Test Fixture

After installation of the solder pads for the springs, a 0.015 in thick block of ULTEM 1000 dielectric was placed on the tip of the post in the text fixture, also using epoxy as the bonding agent. This block will act as a hard stop for the small radius elbow joint, limiting deflection and therefore peak stress magnitude in the joint, and approximating the boundary condition used for initial analysis. ULTEM 1000 was chosen as the constituting material for the joint as RF simulations showed that it was the dielectric with the least losses, showing a negligible effect on the interconnect's gain when radiating an RF signal.

Having adequately prepared the post on the test fixture, the springs could be installed. The initial design involved a set of four springs joined by an upper bare LCP band to be wrapped around the post, with each spring being soldered to its respective pad. A rendering of the spring setup alongside the end result for the first prototype interconnect can be seen in Figure 38. A first prototype using an unplated (bare copper) set of springs was assembled using the wraparound technique, but feedback from the technician that carried out installation prompted for a more time-efficient method. It was very difficult to resolve each 90 degree bend around the post during wraparound, and any initial imprecision in alignment would be propagated more and more as each subsequent spring was wrapped around, and due to the manual nature of the installation, small

imperfections were to be expected even considering the extensive experience of the technicians.

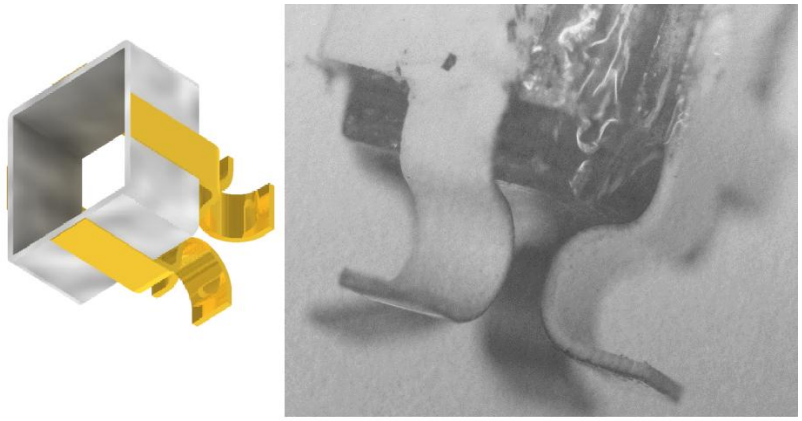

Figure 38: (A) Rendering of the Wraparound Assembly Technique (B) Installed Springs Using Wraparound Technique

It was therefore decided for subsequent prototypes to singulate each spring individually, and install them as separate entities on each pad. Such a setup is still liable to incur in alignment errors, but they would now be random for each spring and not propagated and increased from an initial error. Using the tip of the post as a reference, the mounting height of each spring was carefully verified, and out of the four test runs performed, only one showed a relative misalignment of the springs beyond the 1 mil requirement. The resulting prototype from individual spring installation can be seen in Figure 39.

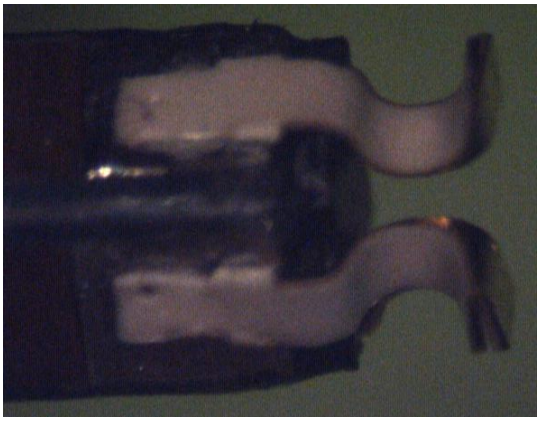

Figure 39: Interconnect Prototype with Individually Installed Springs

Given the difficulty in installation and the requirement for highly skilled technicians to execute the process, neither of the assembly procedures utilized in the prototype manufacturing would be suitable for mass production. While this is not an issue in meeting the primary goals of this investigation, one of the secondary goals which is of interest for future large scale applicability of this concept is indeed mass production. More detail will be discussed in the future work section of this thesis, but a redesign of the assembly procedure is currently underway using the lessons learned from the prototypes in order to better fit this design for mass production. The ideal scenario would be manufacturing a single unit that can just be bonded to the tip of a post and have all alignments ensured, requiring only additional soldering to achieve electrical continuity.

3.6 Conclusions

A manufacturing process was successfully determined and performed using the thermoforming technique to manufacture LCP springs that will be used in a prototype orthogonal interconnect. Using a two-part molding system with a negative half machined from a steel plate and a lightweight positive half with low thermal mass, a forming capability to 0.01” resolution was demonstrated, a first for Harris Corporation. Good resolution without variation in the LCP sheet’s features, such as plating thickness and lamination, relied on smooth geometry transitions in the mold and a proprietary matching of temperature and pressure conditions in the autoclave to keep all parts of the formed printed circuit board below the glass transition temperature of the LCP blend used. Furthermore, an assembly method was developed to mount the springs onto a post with all ancillary hardware for use in the experimental setup. While the assembly allowed for limited prototype fabrication, it was not deemed ideal for large scale production due to the significant amount of specialized manual labor involved, which has opened the door for further investigation to meet the secondary objective of mass producibility.

CHAPTER 4

EXPERIMENTAL PERFORMANCE VALIDATION

4.1 Setup Requirements, Component Selection, and Fabrication

To accurately validate the predicted performance of the interconnect, an experimental setup must be designed that allows monitoring of the interconnect during cyclic loading, identifying the time of failure and failure mode. The primary requirement for this setup is run time: 10^7 cycles, the survivability outlined in the primary success criteria, must be achieved in the order of hours, to allow testing of multiple prototypes in both axial and horizontal loading during the allocated testing time. In this manner, random errors due to possible manufacturing defects can be identified, leading to the computation of an average value for the number of cycles to failure in each excitation direction. Further requirements for the setup are outlined in Table 1.

Table 1: Design Requirements for the Experimental Setup

Excitation Type	Axial and Horizontal
Excitation Amplitude	0.004” preload $\pm$ 0.004” cyclic load amplitude
Excitation Control	Open loop with amplitude verification
Time to Completion	Order of Hours
Alignment Adjustability	3 DoF translation and 3 DoF rotation
Monitoring	Continuous with failure point identification

The best candidate to provide the required excitation amplitude at the desired frequency is a permanent magnet shaker system, specifically an LDS V203 unit from Bruel and Kjaer, which has ideal displacement capabilities for this application. The V203 includes a 10/32-UNF threaded hole in its head, allowing for the mounting of several instruments and fixtures. This mounting point was used to design and fabricate an adapter fixture which would contain the interconnect and mount to the shaker. The adapter is composed of two parts with a cylindrical base: a base plate with a concentric 10/32-UNF threaded

stud and two bonded #4 threaded fasteners that serve as aligning and securing features for the secondary plate with a protruding post on which the interconnect is mounted. The assembly is shown in Figure 40 and includes a conductive copper trace with solder pads on each side of the post to which the interconnect and lead wires for signal monitoring are soldered. Both components were machined out of mild steel. The two grooves on the secondary plates allow for 90 degrees of rotation adjustability after mounting to the shaker, ensuring proper alignment of the setup. For horizontal testing, a new secondary plate was machined in which the post executes a 90 degree bend and extends to clear the fixture. A rendering of the horizontal test fixture is shown in Figure 41.

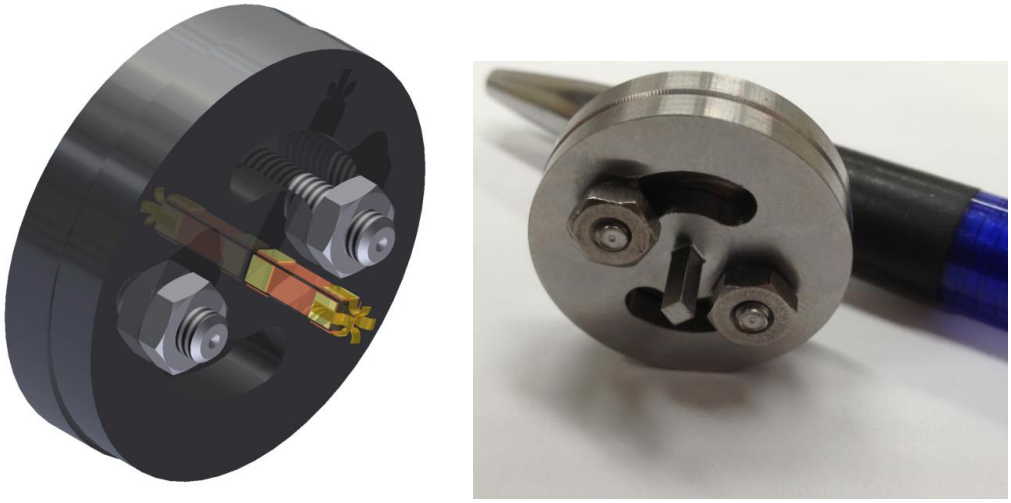

Figure 40: Machined Two-Part Shaker Adapter (right) and Rendered Interconnect Assembly on the Adapter (left)

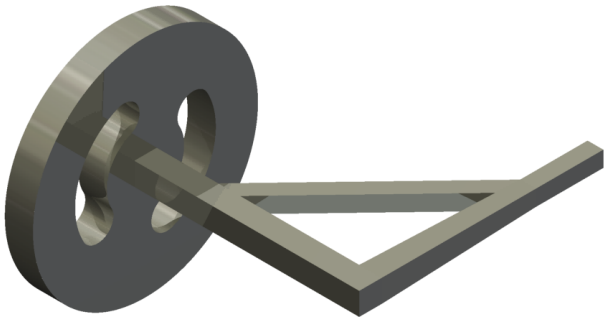

Figure 41: Rendering of the Secondary Adapter Plate for Horizontal Fatigue Testing

Due to the horizontal test fixture having a long and slender post in order to clear the shaker, and the excitation being harmonic, the modal behavior of the fixture had to be taken into consideration to ensure that the interconnect did not receive any additional or modified loading from the imparted excitation. The solid model of the fixture was imported into COMSOL and a modal analysis was performed with cantilevered boundary conditions, with the fixed end being the rear face of the circular plate simulating attachment to the shaker. The stiffening cross-member shown was added subsequently to ensure that the first mode of the fixture was above 1000 Hz, well beyond the excitation frequency range being used in this setup. To increase stiffness, the two right-angle posts also have a higher cross-sectional area, tapering to the area of a typical interconnect application, and equal to that of the axial test fixture, at the tip. The first mode of the fixture's response to harmonic excitation is shown in Figure 42.

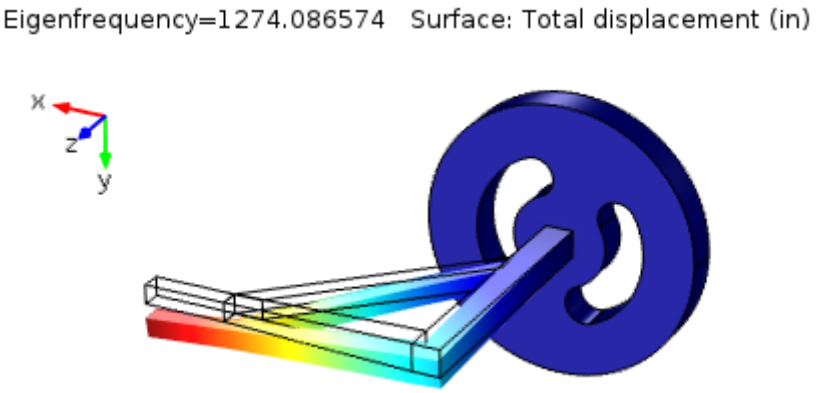

Figure 42: First Mode of the Horizontal Test Fixture at 1.2 kHz from COMSOL Simulation

In order to continuously monitor interconnect performance throughout the test, a DC voltage will be fed through the interconnect via the solder pad connection points on the post. The interconnect will then mate to a perpendicular printed circuit board with copper traces corresponding to each spring finger, from which the signal will be retrieved via a further set of lead wires. A digital logic circuit was devised to identify time of

failure, the details of which will be addressed in the following section. Discussion on component selection and fabrication has been so far centered on the interconnect side of the setup, and the mating board side will now be discussed. The board was manufactured on a 3x3 inch FR-4 dielectric layer on which copper traces were printed using a photoetching process, one for each spring finger. The traces were then plated with Electroless Immersion Nickel-Gold (ENIG) and allow for soldering of lead wires on the external edges. Four ¼" diameter alignment holes were drilled 2 inches apart in the dielectric for mounting on an optical stage. The board is shown in Figure 43.

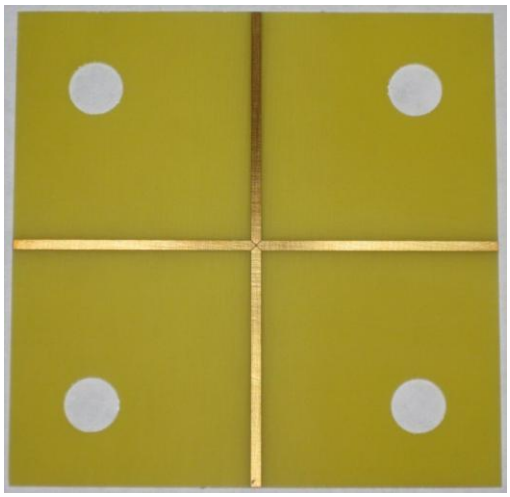

Figure 43: Mating Side Printed Circuit Board for Axial Testing

As discussed previously with regards to the modal behavior of the horizontal test fixture for the interconnect, obtaining a first natural frequency for the fixture that was greater than 1000 Hz was of paramount importance to ensure the validity of test results. The modal response shown is for the final design configuration, and one of the important parameters in determining the first natural frequency, together with the stiffening cross member added, is the length of the post that protrudes perpendicularly from the shaker. Using the mating board designed for axial testing would require too long of a post extension, requiring significant design challenges to obtain the required modal response. Therefore, a new mating board design was created for horizontal testing, in which the pad

geometry was repeated at the end of each trace, allowing for a shorter post to obtain contact and also ensuring redundancy from manufacturing defects as four attachment points were available. All external dimensions and mechanical features such as locating holes are unchanged, and the base material remains FR-4 dielectric. The new mating board for horizontal testing can be seen in Figure 44, with the trace extensions to the edges of the board being necessary for the plating process.

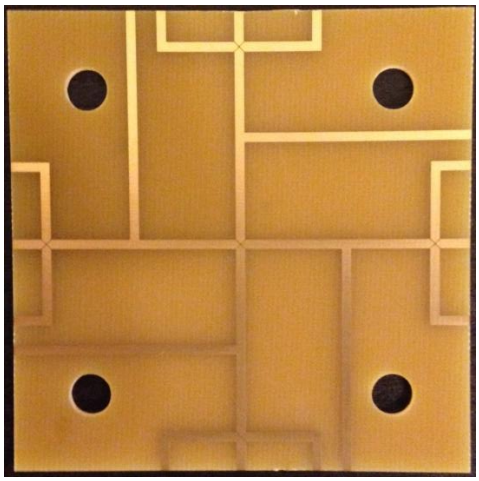

Figure 44: Mating Side Printed Circuit Board for Horizontal Testing

In the final test setup, both boards are mounted onto a 90 degree angle bracket which is then secured on a two degree of freedom optical stage, fixed to an optical table with high frequency passive stabilization. All hardware is produced by Newport Optics. The stage allows for translation in the plane of the table, while vertical adjustment is provided by placing shims under the shaker mounting trunnion. The planar translation is especially important not only for aligning the two components of the test setup, but also for determining the preload on the interconnect springs. Contact between the spring fingers and the mating board can be identified when DC continuity between the two components is achieved, and from there the desired preload can be applied by further displacing the mating board with the axial stage controlling motion in the axial direction, which is conveniently marked in 0.001” increments. A side view rendering of the

completely assembled test setup, is shown in Figure 45 for ease of visualization, while the actual setup is shown in Figure 46.

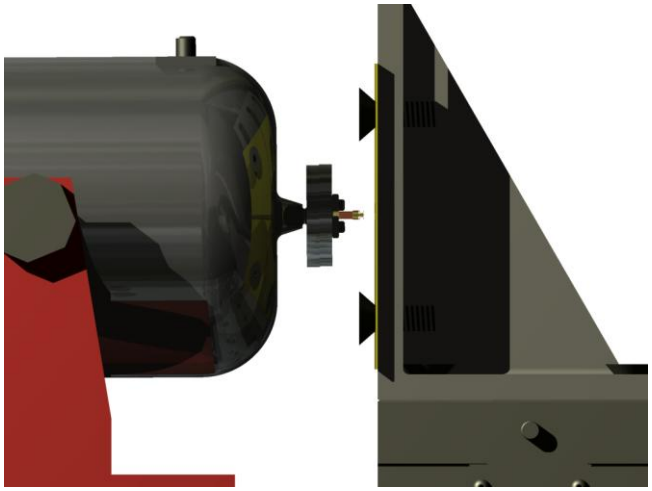

Figure 45: Side View Rendering of Assembled Unmated Experimental Setup

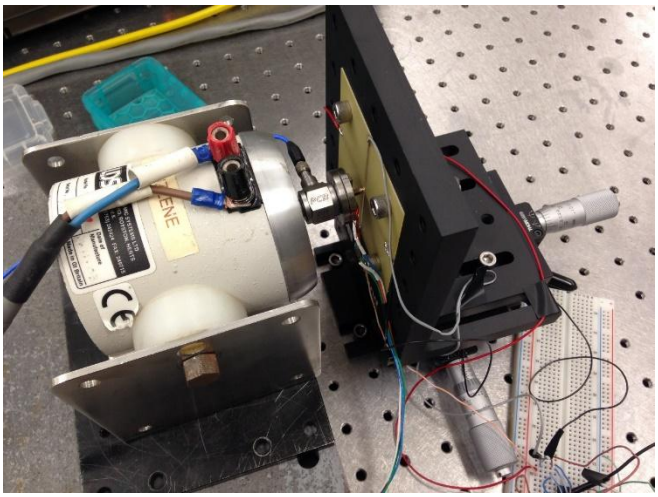

Figure 46: Experimental Setup, Mated with All Components in Operation

As far as control of rotational degrees of freedom, the interconnect mounting fixture allows control of the in-plane alignment between the spring fingers and their respective traces, the shaker mounting trunnion allows for adjusting the pitch angle of the fixture relative to the mating board, and yaw angle relative to the board is controlled manually by rotating the entire shaker assembly. Rotational control is essential in ensuring that all springs are subject to even loading, and attention was paid to align the setup such that contact of all springs occurred within 0.001” of the first spring’s contact.

4.2 Digital Acquisition Logic

In order to accurately determine the time of failure of the interconnect, a simple digital logic circuit was implemented using an AND gate. As stated previously, a 5V signal was fed from a DC Power Supply to the interconnect via lead wires soldered to the post fixture, one for each individual spring. The springs are then mated to their respective trace on the perpendicular mating board, which also contains a lead wire for each trace. The signal from the traces is then fed through an AND gate, and the resulting DC signal is monitored by a National Instruments USB Data Acquisition System. Failure of any of the springs will sever continuity in that lead, and cause the AND gate to return a logic low (approximately 0.14 V) allowing identification of the time of failure from the time series recording. Since the excitation is performed at constant frequency, knowing the time of failure the run time can be calculated and therefore the number of cycles to failure. The voltage output from the logic gate is also used as a triggering condition, terminating excitation if it falls below 1 V. A diagram of the acquisition logic is shown in Figure 47.

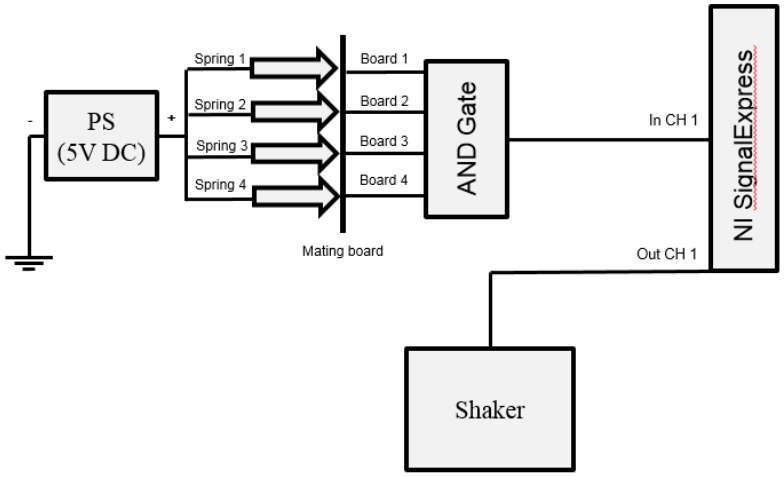

Figure 47: Digital Acquisition Logic Diagram for Experimental Setup

The National Instruments DAQ was also used to monitor two other sensors used to monitor the setup's performance: a load cell is placed between the shaker head and the

interconnect mounting fixture to determine the spring load on the system due to cyclic loading, and an accelerometer is placed on the interconnect fixture to verify the appropriate cyclic load is being imparted, as will be explained in the following section covering the excitation setup. The acquisition setup is therefore operating with four channels: three inputs (logic gate voltage, shaker head axial acceleration, and spring load) and one output (voltage to shaker). All acquisition logic, input monitoring, and excitation setup is implemented in the National Instruments SignalExpress digital acquisition software. A complete circuit diagram of the interconnect monitoring circuit is shown in Figure 48 as constructed on an electrical breadboard, with pinouts of the logic gate as used for a Texas Instruments 74AS21 4 input AND gate. The diagram shows pull-down resistors at the logic gate input locations for proper operation of the gate.

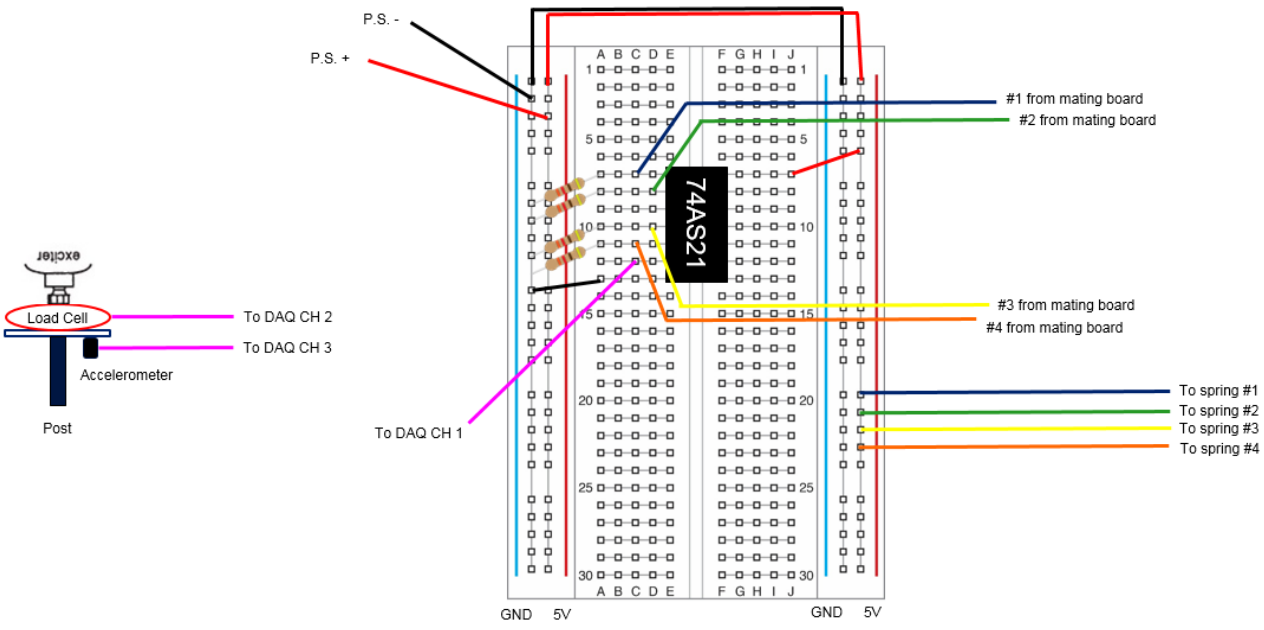

Figure 48: Breadboard Schematic of Acquisition Logic Circuit and Monitoring Sensors

4.3 Excitation Setup and Monitoring

The excitation for cyclic loading of the interconnect is provided by the LDS V203 shaker and commanded by SignalExpress through the DAQ board's only available output channel. The excitation was chosen to be sinusoidal, which grants two advantages. The main advantage is that with harmonic excitation, knowing the run time of the experiment until failure allows for easy determination of the number of cycles to failure, by simply multiplying the run time in seconds by the excitation frequency in Hertz. Furthermore, we can then use the equations of simple harmonic motion to derive the acceleration amplitude of a particle undergoing sinusoidal motion. The relation is outlined in Equation 6.

$$A = \frac{2\pi^2 F^2 D}{G} \qquad (6)$$

In the equation above, F represents the frequency in Hertz, D the peak-to-peak displacement in inches, and G is a constant equal to 386 in/s^2. Even though the excitation will not have a closed loop controller to maintain the desired displacement amplitude, assuming a constant voltage is supplied by the DAQ with no large fluctuations, the displacement can be verified by observing that the accelerometer is recording the correct acceleration amplitude throughout the test. For the purpose of this experiment, an excitation frequency of 230 Hz was chosen, as a compromise between run time and required voltage to achieve the desired cyclic displacement amplitude. Runs were also performed at 300 Hz but the lower frequency was chosen due to the voltage amplitude required to obtain a cyclic displacement amplitude of 0.004" being close to the maximum allowed voltage for the shaker. At 230 Hz, substituting all known terms into Equation 6, the corresponding peak acceleration is 19.7 G. This value was used to tune the voltage

amplitude supplied to the shaker and ensure the desired cyclic displacement was obtained. The excitation setup for axial loading is summarized in Table 2.

Table 2: Summary of the Excitation Setup for Axial Loading

Excitation Type	Sinusoidal
Excitation Frequency	220 Hz
Excitation Amplitude	± 0.004”
Spring Preload	0.004”
Peak Acceleration	19.79 G

The typical loading case for horizontal fatigue for the given application assumes the same spring preload but half of the cyclic load. The excitation setup for horizontal loading is therefore summarized in Table 3.

Table 3: Summary of the Excitation Setup for Horizontal Loading

Excitation Type	Sinusoidal
Excitation Frequency	220 Hz
Excitation Amplitude	± 0.002”
Spring Preload	0.004”
Peak Acceleration	9.87 G

4.4 Results: Performance Under Axial Cyclic Loading

The fatigue test was run in four different cases in axial mode. All samples were analyzed under a microscope at 4x magnification after each run, to identify the failure mode that lead to loss of electrical continuity between the post and the mating board. An initial run in axial loading was performed with a bare copper interconnect, where the springs did not undergo hard nickel-gold plating. This was done in order to experimentally observe the effect of the plating layers on the fatigue life of the connector, as well as validate the FEM predictions of peak stress magnitude and subsequent fatigue resistance. Comparing performance with and without plating also allows greater

flexibility to refine the design in order to further improve the springs' mechanical performance under cyclic loading. The bare copper interconnect achieved 15 million cycles before continuity was lost. Upon further inspection, one of the thin wires carrying the DC signal from the leads on the breadboard to the solder pads on the post severed off during the test. Inspection of the interconnect under 4x magnification showed no damage to the springs aside from slight wear of the copper layer from metal-to-metal contact with the mating board during cyclic loading. The lack of crack initiation allows speculation that the interconnect can survive a significant number of further cycles, as well as confirms that significantly lower peak stresses are encountered without the plating layers, due to the thickness dependency of the stress distribution in the connector geometry. The condition of the copper springs can be seen in Figure 49.

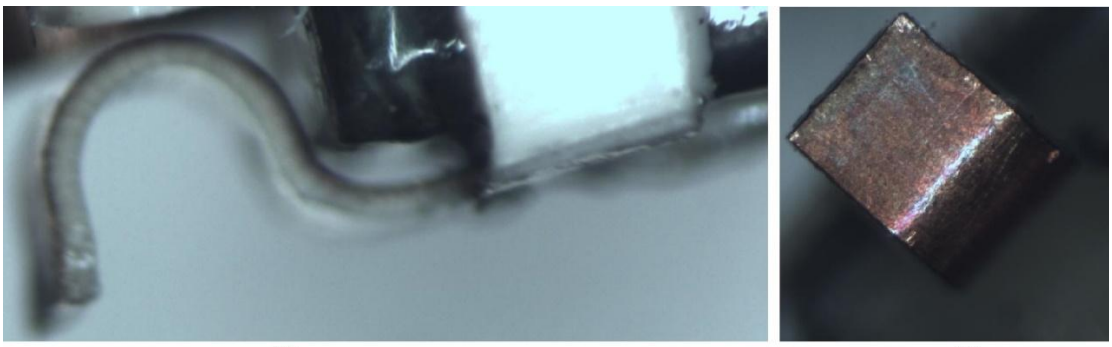

Figure 49: Condition of a Single Copper Spring After 15 Million Cycles of Axial Loading at 4x Magnification. (a) Side View Showing No Damage to Metallic Layer, (b) Top-Down View Showing Wear

The test fixture was subsequently re-fitted with a Nickel-Gold plated interconnect and the experiment reset for a new run. During alignment of the shaker and mating board, a manufacturing defect was noted where the springs on the interconnect were not of even height, and could not be mated with less than a 0.005" error between their relative contact pre-loads. It was decided to run the test regardless to obtain a worst case scenario estimate, as the tallest spring would sustain a significantly larger preload than the typical operational condition. Failure occurred in the tallest spring, as expected, after 7 million

cycles. The fitting issue was discussed and resolved with Harris, which provided a new Nickel-Gold plated sample that was then mated within the desired tolerance of 0.001" between the springs' relative moment of contact with the mating board. The correctly aligned interconnect survived 18 million cycles before continuity was lost in one spring. Both cases were analyzed under 4x magnification and cracks were found on the failed springs at the midpoint of the large radius. Crack location and cycle count order of magnitude confirm the FEA model predictions. It was observed in the interconnect that underwent 18 million cycles to failure, that the crack does indeed originate in the gold layer and from the edge of the spring inwards, but propagates through all metallic layers once it spans the entirety of the spring width, severing continuity. An image of the crack location and propagation through all layers in the failed spring can be seen in Figure 50, while crack initiation in the gold layer (circled) can be observed in Figure 51. It must be noted that with the crack only present in the gold layer, DC continuity throughout the spring was maintained, therefore the spring fails due to loss of continuity only when the crack has completely propagated through all conductive metallic layers, down to the LCP. Visual observations under the microscope and probing with a multimeter in continuity monitoring mode also showed no damage to the small bend radius, confirming proper functioning of the dielectric hard stop in reducing deflections at the elbow joint, keeping stresses below the fatigue strength of all metals used. Furthermore, no damage to the LCP base material was observed.

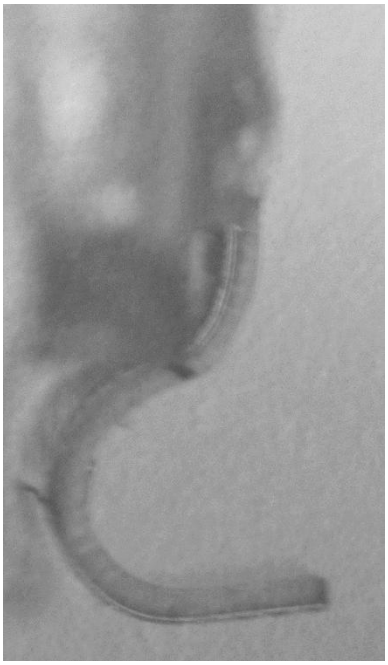

Figure 50: Side View of Failed Plated Spring after 18 Million Cycles at 4x Magnification

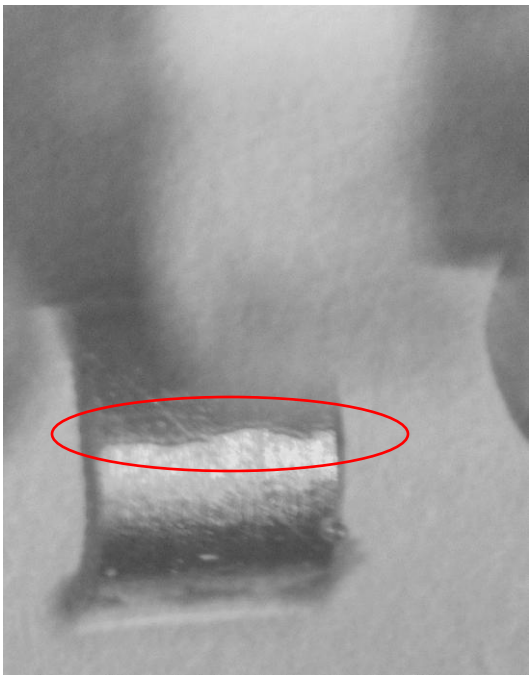

Figure 51: Back View of Crack (Circled) Initiating in the Gold Layer of a Spring after 18 Million Cycles at 4x Magnification

Finally, a new Nickel-Gold plated interconnect was tested at a reduced cyclic deflection, to quantify the sensitivity of fatigue life to the combined deflection under load. Preload was maintained at 0.004" but the cyclic deflection was reduced to 0.002". The interconnect was removed from the test setup after 36 million cycles for visual observation and no significant damage was found, with continuity being present in all springs. A summary of axial testing and results can be seen in Table 4. The new interconnect design provides a 2 order of magnitude increase in fatigue life at operational conditions, and a 1 order of magnitude increase under worst case conditions.

Table 4: Summary of Axial Testing Results

Interconnect Type	Preload	Cyclic Load	# Cycles	Failure	Failure Mode	Notes
Bare Copper	0.004"	± 0.004"	15 Million	No	N/A	Lead Wire on Post Broken
Plated	0.004"	± 0.004"	7 Million	Yes	Cracking of Metallic Layers at Peak Stress Location	Unbalanced Spring Height. Maximum Differential 0.005"
Plated	0.004"	± 0.004"	18 Million	Yes	Cracking of Metallic Layers at Peak Stress Location	
Plated	0.004"	± 0.002"	36 Million	No	N/A	Removed From Setup for Observation

An interesting observation was made with regards to the effects of metal-to-metal contact, specifically when both surfaces are plated with gold, which has a high coefficient of friction. Just as wear in the top metallic layer was observed on the spring side of the test setup, similar wear patterns were also found on the mating board at the points where

the interconnect made contact. The original design for the mating board shown in Figure 43 was manufactured with an ENIG plating, resulting in a very thin layer gold plating layer. After about 25 million cycles on the mating board combined between several test runs, the interconnect wore through the gold layer down to the underlying nickel layer, over which an oxide layer was quickly formed as it became exposed to atmospheric conditions. This can be seen in Figure 52 as the dark spots appearing on the traces. The resulting nickel oxide is non-conductive, and continuity was severed.

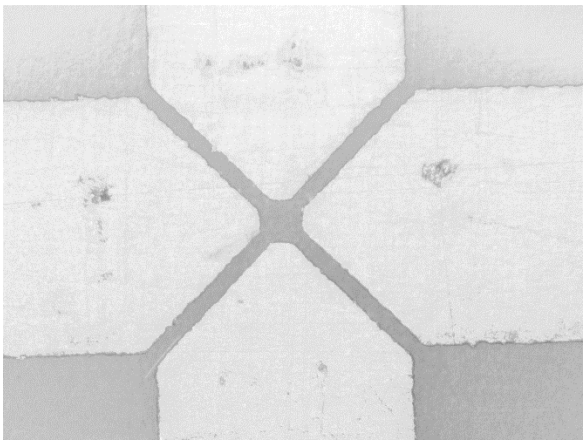

Figure 52: Condition of the Mating Board After a Combined 25 Million Cycles at 4x Magnification.

This observation was made after a loss of continuity was reported by the setup, but the individual springs retained continuity with their respective lead wires when tested with a multimeter. However, there was no continuity between the contact points on the mating board and their respective lead wires, which triggered the setup to stop as programmed. To avoid repetition of this problem, which would add uncertainty to the experimental results as the interconnect would have to be re-mated with the board upon its substitution, a new board was manufactured incorporating hard electrolytic nickel-gold plating, with the same thicknesses as the springs themselves: 200 µin of nickel and 50 µin of gold.

4.5 Results: Performance Under Horizontal Cyclic Loading

After completion of the axial tests, the horizontal adapter was installed on the shaker with a gold plated interconnect to verify its performance to transverse vibrations. As stated in the excitation setup description, a typical operational environment would involve transverse vibrations with half the cyclic amplitude of the axial vibrations, therefore the excitation amplitude was set at $\pm$ 0.002" while retaining the same 0.004" preload. Continuity was maintained by all springs up to 80 million cycles, after which the test was stopped as the appliance had more than exceeded both primary and secondary goals for this investigation. Wear of the metallic surfaces was an initial concern due to the observations made during axial testing, but the revised mating board with thicker gold plating proved effective. Upon visual observation of the board after 80 million cycles, a wear pattern was visible but the gold thickness was sufficient to warrant wear down to the nickel layer. The condition of the board can be seen in Figure 53, with the worn areas circled for clarity due to the lower contrast of the imaging device used.

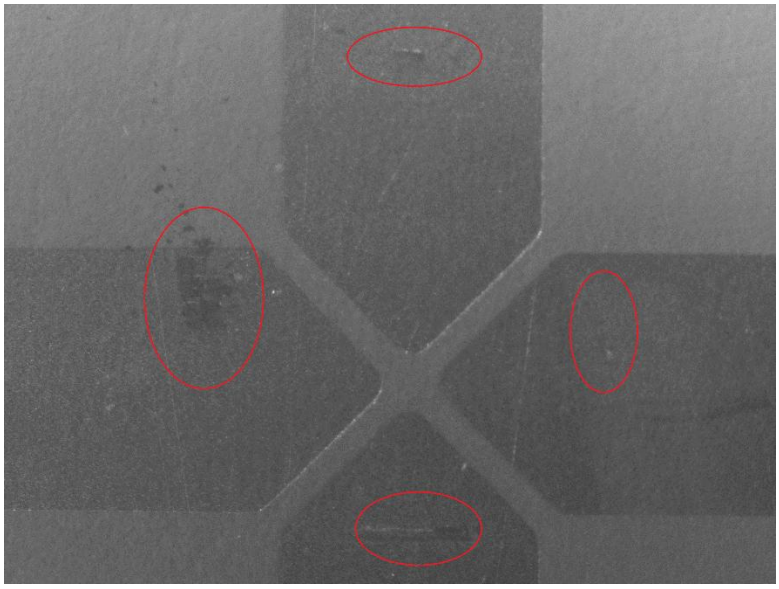

Figure 53: Condition of the Revised Electroplated Mating Board after 80 Million Cycles in Transverse Excitation at 4x Magnification

The interconnect springs also exhibited some wear of the gold surface, and while clearly greater than after 15 million cycles as shown in Figure 54, does not call for concern for a future loss of continuity due to wear.

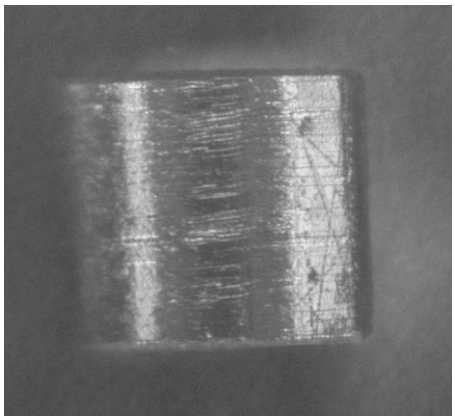

Figure 54: Top-Down View at 4x Magnification of a Single Spring Showing Gold Wear after 80 Million Cycles in Transverse Excitation

A summary of testing in transverse excitation is given in Table 5.

Table 5: Summary of Horizontal Testing Results

Interconnect Type	Preload	Cyclic Load	# Cycles	Failure	Failure Mode	Notes
Plated	0.004”	$\pm$ 0.002”	80 Million	No	N/A	Removed From Setup for Observation

4.6 Conclusions

A test setup was successfully designed and implemented for the testing of orthogonal interconnects for high cycle fatigue, using DC continuity monitoring to determine number of cycles to failure and allowing for subsequent visual observation to determine failure mode. Testing times are significantly shortened compared to industry standard, allowing testing to failure within the order of hours. Axial testing of the proposed LCP interconnect showed failure at 18 million cycles for the standard 4 mil preload $\pm$ 4 mil cyclic loading scenario when gold plated, while a bare copper version

was seen to be potentially more resilient, showing no signs of damage after 15 million cycles for the standard loading scenario, although the test had to be interrupted due to a failure of the fixture. While the gold plated results meet and exceed the primary goal for this investigation, the copper results show a potential for improvement on the design's performance by modifying the plating composition and distribution on the interconnect springs. Peak stress dependence on plating was initially determined analytically, matched numerical results and is now confirmed experimentally. Horizontal testing yielded no damage after 80 million cycles, meeting and exceeding both primary and secondary objectives. An unexpected failure mode was encountered through wearing of the gold layer on the mating board side of the setup, resulting in a non-conductive Nickel Oxide layer at the contact point due to friction from metal-to-metal contact. This failure mode was avoided in all future iterations of the experiment by modifying the mating board design, from an ENIG plating to a hard Nickel-Gold plating with a 5 µIn top layer of gold.

CHAPTER 5

CONCLUSIONS AND FUTURE WORK

5.1 Summary

The problem of orthogonal interconnection for RF circuits at the board level presented many challenges throughout all phases of development, particularly when stringent mechanical requirements are introduced on such a small, load bearing device that will be subject to high cycle fatigue.

From the design point of view, a geometry must be designed to join two perpendicular surfaces using a smooth curve that will not present stress discontinuities and not exceed the fatigue strength of the constituent materials at the desired cycle count, as well as utilizing materials that allow for manufacturing of the design. Utilizing Copper-clad LCP allowed to meet these mechanical performance goals, and also provided adequate RF performance as shown from RF testing performed by McQuaide, Khan, Guidoni, Ruzzene, and Papapolymerou [4] as part of this research effort which for the first time demonstrated the RF feasibility of an orthogonal interconnect at the board level.

Manufacturing of a prototype also proved difficult due to the novel processes involved. One of the driving parameters that lead to the choice of LCP as a constituent material for the interconnect springs was the ability to thermoform the base material into complex geometries. However, within Harris Corporation, thermoforming of LCP had never been performed to such a small feature size. After initial successes with breadboard runs in forming small radius semicircles, down to 0.01 inches, the tooling selected for forming of the spring appliance was not able to correctly resolve the geometry without

causing damage to the base material. A hybrid approach was subsequently implemented incorporating a method similar to that of the breadboard runs that allowed to form the LCP to the desired geometry with no damage or modification to any of the material's layers.

Finally, a test setup was designed and implemented to allow for high cycle fatigue testing of interconnects in the order of hours, significantly reducing testing time compared to many state of the art test setups used in industry. The setup used DC continuity monitoring by feeding a DC current through the interconnect and retrieving it from a circuit board to which the interconnect mates, simulating an orthogonal connection between a post and an antenna board. Excitation was performed at a constant frequency and the voltages retrieved from each contact point were compared through an AND logic gate. Failure of any of the springs would return a logic low and the test would stop. Comparison of run time with excitation frequency was able to yield an accurate cycle count on the appliance before failure. The interconnect prototype was able to survive 18 million cycles of axial deflection under a typical load scenario of 4 mil preload and 4 mil cyclic load amplitude. Horizontal deflection did not affect the interconnect significantly and does not pose a threat to survivability of the appliance. It must be noted that, while the interconnect's performance exceeded the primary goal of this investigation, it did not reach the secondary goals of 35 million cycles, which would be preferable for a mass produced appliance used in industry. The springs also proved to be very susceptible to initial alignment, setup, and deflection, showing differences up to several million cycles to failure based on how the test was initialized. Overall, this investigation demonstrated for the first time a functioning orthogonal interconnect for RF

circuits at the board level, and provided a prototype that was able to survive high cycle fatigue to the order of 10^7 cycles. While the prototype appliance served as a successful proof of concept, there are several refinements that must be made for such an appliance to be reliable and suitable for mass production in industry applications.

5.2 Contributions

The design portion of this investigation identified a geometry that could effectively bring the capability of orthogonal interconnection at the board level to RF circuits, using a semicircular arc that met all mechanical requirements and did not increase insertion and return losses. This geometry was successfully adapted to fit the mounting requirements in a way that satisfied manufacturing constraints but did not substantially change the boundary conditions of the real appliance compared to the FEA simulations used to predict performance. This interconnect was able to survive cyclic loading under high cycle fatigue conditions within the order of magnitude of 10 million cycles, which represents a typical industry application, but failed to reach the exact cycle count of 35 million. . An invention disclosure has been submitted and is currently under review.

In the studies performed on thermoforming to manufacture an initial prototype, a contribution to the state of the art of thermoforming within Harris was also made: demonstrating the feasibility of LCP thermoforming to a feature size of 0.01 inches using simple two-part mold tooling.

From the experimental point of view, a contribution was made in the realm of testing with the development of an experimental setup to test orthogonal interconnects to the order of tens of millions of cycles within hours by exciting at over 200 Hz, while

monitoring electrical continuity through the appliance to determine the instant of failure and subsequently stop testing. Visual observations under a microscope can then be performed to identify failure mode. The setup is very versatile and allows for testing of many different interconnect designs due to a fixture simulating a post on the vertical card that can quickly be disconnected and fitted with a new design. This represents a significant improvement over the previous Harris test process which could only excite the interconnect at 1 Hz, employing days or even weeks to reach the desired cycle count.

5.3 Future Work

In order to open the door to orthogonal interconnection in mainstream RF circuit design, the scope of this investigation must be widened to allow for development of a design that can be mass produced and is reliable to industry standards. From the performance point of view, there are several directions that can be taken to improve the interconnect's performance beyond the 35 million cycles required by industry under the typical load case. The first, and simplest solution involves no geometric changes to the appliance, but focuses on the plating layers. It has been shown from the design phase that peak Von Mises stresses in a layer are directly proportional to the layer's thickness. Since failure of the appliance occurred starting from the gold layer, as predicted by simulation, a possible solution would be to selectively plate the interconnect based on where environmental protection was necessary. One option discussed would be to Nickel-Gold plate only the two contact points at the extremities of the spring, leaving the remaining section of the interconnect, which includes the peak stress location, as bare copper. The unplated interconnect showed significantly better fatigue performance under testing, and oxidation of the copper layer in a location that does not function as a contact between two

surfaces does not impact RF performance. A second batch of selectively plated prototypes could be produced using existing tooling and tested using the current test setup to verify any increase in performance from plating variation.

A more complex expansion of scope involves focusing more on the optimization aspect of this investigation. Circular arcs were chosen as the baseline geometry as they provided smooth transitions between two perpendicular planes and allowed for analytical solutions to their stress distribution. Our basic optimization allowed to identify the driving parameters to minimize the stress distribution, but were still constrained to the analytical geometry chosen. This minimization technique could be expanded to include the FEA models, by coupling COMSOL with the optimizer through a MATLAB interface. By doing so, the stress distribution could be minimized based on the Finite Element solutions, and would lift any restriction on employing an analytical geometry. A good geometry that could be optimized given the spatial constraints of the problem is Bezier curves. Four points that define the spatial restrictions could be initialized and a Bezier curve generated. An interesting result would be to see the effect of the Bezier curve's order on the stress distribution within a spring with non-analytical geometries.

REFERENCES

[1] PETIT, A., PENICAUD, E., LE GOZ, G., & JAMET, D. (1987). U.S. Patent No. 4,703,394. Washington, DC: U.S. Patent and Trademark Office.

[2] STILLIE, D. G. (1987). U.S. Patent No. 4,693,529. Washington, DC: U.S. Patent and Trademark Office.

[3] KWONG, H., NGUYEN, B. C. L., AU, V. C., SENYSHYN, P. A., HANDFORTH, M. R., MEIER, R. G., ... & HAYES, H. R. (2002). U.S. Patent No. 6,462,957. Washington, DC: U.S. Patent and Trademark Office.

[4] GOVERDHANAM, K., SIMONS, R. N., & KATEHI, L. P. (1999). Novel three-dimensional vertical interconnect technology for microwave and RF applications (pp. 641-644). National Aeronautics and Space Administration, Glenn Research Center.

[5] NEWMAN, M. W., MUTHUKUMAR, S., SCHUELEIN, M., DAMBRAUSKAS, T., DUNAWAY, P., JORDAN, J. M., ... & WORWAG, W. (2006). Fabrication and electrical characterization of 3D vertical interconnects. In Electronic Components and Technology Conference, 2006. Proceedings. 56th (pp. 5-pp). IEEE.

[6] DAVIS, W. R., WILSON, J., MICK, S., XU, J., HUA, H., MINEO, C., ... & FRANZON, P. D. (2005). Demystifying 3D ICs: the pros and cons of going vertical. Design & Test of Computers, IEEE, 22(6), 498-510.

[7] QIU, J., KAWAGOE, M., MIZUNO, W., & MORITA, M. (2001). Effect of LCP Addition Content on the Microstructure and Fatigue Property of PP/LCP Polymer Blends. In Transactions of the Japan Society of Mechanical Engineers Series A vol. 67 (pp. 704-710)

[8] SLOAN, F., BULL, S., & LONGERICH, R. (2005). Design Modifications to Increase Fatigue Life of Fiber Ropes. In *OCEANS, 2005. Proceedings of MTS/IEEE* (pp. 829-835). IEEE.

[9] VOSS, H., & FRIEDRICH, K. (1986). Influence of Short-Fibre Reinforcement on the Fracture Behaviour of a Bulk Liquid Crystal Polymer. *Journal of materials science,21*(8), 2889-2900.

[10] THOMPSON, D., KINGSLEY, N., WANG, G., PAPAPOLYMEROU, J., & TENTZERIS, M. M. (2005, June). RF characteristics of thin film liquid crystal polymer (LCP) packages for RF MEMS and MMIC integration. In Microwave Symposium Digest, 2005 IEEE MTT-S International (pp. 4-pp). IEEE.

[11] DEAN JR, R. N., WELLER, J., BOZACK, M., FARRELL, B., JAUNISKIS, L., TING, J., ... & HETKE, J. (2004, October). Novel biomedical implant interconnects utilizing micromachined LCP. In Optical Science and Technology, the SPIE 49th Annual Meeting (pp. 88-99). International Society for Optics and Photonics.

[12] HA, D., KIM, B. G., LIN, T. Y., OUYANG, Y., IRAZOQUI, P. P., & CHAPPELL, W. J. (2010, May). 3D packaging technique on liquid crystal polymer (LCP) for miniature wireless biomedical sensor. In Microwave Symposium Digest (MTT), 2010 IEEE MTT-S International (pp. 612-615). IEEE.

[13] MCQUAIDE, D., KHAN, W., GUIDONI, L., RUZZENE, M., & PAPAPOLYMEROU, J. (2014, October). Orthogonal Wideband (DC-10 GHz) Microstrip-to-Microstrip Transition Using Flexible LCP Interconnects. In European Microwave Conference (EuMC), 2014 44th (pp. 1781-1784). IEEE.

[14] YOUNG, W. C., & BUDYNAS, R. G. (2002). Roark's formulas for stress and strain (Vol. 7). New York: McGraw-Hill.

[15] VELAZQUEZ, E., & KOSMATKA, J. B. (2013). Stresses in Half-Elliptic Curved Beams Subjected to Transverse Tip Forces. Journal of Applied Mechanics, 80(1), 011010.

[16] MOGILEVSKY, M., SIEGMANN, A., & KENIG, S. (1998). Thermoforming of liquid crystalline polymer sheets. Polymer engineering and science, 38(2), 322.

[17] SUN, T., DATTA, A., DE SOUZA, J. P., & BAIRD, D. G. (1991). Thermoforming of Insitu Reinforced Thermoplastic Composites. VIRGINIA POLYTECHNIC INST AND STATE UNIV BLACKSBURG POLYMER MATERIALS AND INTERFACES LAB.